

# **The Distribution of Saturated Clusters in Wetted Granular Materials**

**By**

**Shuoqi Li**

A thesis submitted in fulfilment of the requirements for the degree of

**Master of Philosophy**

Faculty of Engineering and Information Technology

The University of Sydney

2017



*To my great parents, Jianhua and Peiyi.*

*For having nourished me with curiosity for a whole lifetime.*

*For having given me unconditional support.*

*For having taught me all the important things.*



# Acknowledgements

Possibly the most important personal outcome of my MPhil is knowing how to ask for help. Experimental research needs vast endeavour and in order to progress one needs proper support. I am extremely grateful to find in my early-stage academic career some truly great people who I could not have done this without.

I would first count my supervisor Dr. Yixiang Gan, in The University of Sydney, among these people. The everyday unabridged friendly communication with him is the main contributor to our excellent interaction. I honestly think that I am not the only person who feels this way. From our interactions, his research experience in this field and valuable ideas tremendously influenced me and helped me open the avenue for my career path. I am thankful that I have crossed paths along with him and have already benefited a lot from these two years of study.

Along with Yixiang, I need to express my gratitude to Dr. Dorian Hanaor from Technische Universität Berlin. Dorian acted as another supervisor to me. He spent a vast amount of time and energy to help me with my academic writing skills.

As mentioned before, the experimental research is a collaborative path. I overcome many technical challenges in the past two years and received encouragement and help from our team members, among which I would like to mention Chongpu Zhai and Weijing Dai. Their help is essential for me to accomplish this study.

Finally I would like to express my gratitude to my family in China. It is their unconditional support that encourages me to go further. And their attention on my study is the most valuable gift I could possibly ask for.

# Notation

The following is a list of the symbols used in this thesis.

$\gamma$	Interfacial energy (mN/mm <sup>2</sup> )
Ca	Capillary number
Bo	Bond Number
$r$	Radius of meniscus curvature (mm)
$\theta$	Contact angle (°)
$K$	Hydraulic conductivity (mm/s)
$\mu$	Viscosity (mPa·s)
$\rho$	Density (g/cm <sup>3</sup> )
$R_0$	Radius of curvature at the drop apex (mm)
$d_e$	Maximum diameter of pendant drop (mm)
$d_s$	Diameter at the distance of the maximum diameter $d_e$ from the drop apex (mm)
$\beta$	Shape factor of a pendant drop
$D_n$	Diameter of the needle (mm)
$g$	Gravitational acceleration (m/s <sup>2</sup> )
$a$	Typical pore size (mm)
Bo*	Generalised Bond number
$N_s$	Number of square boxes interested by the image in boxing counting method
$s$	Side length of the squares in boxing counting method
$D$	Fractal dimension
$V_V$	Total volume of voids (mm <sup>3</sup> )

$V_w$	Total volume of water (mm <sup>3</sup> )
$n$	Porosity
$\varepsilon_i$	Strain component
$\sigma'_i$	Principal effective stress component
$E$	Young's modulus (kPa)
$\mu'$	Poisson's ratio
$u_a$	Pore air pressure (kPa)
$u_w$	Pore water pressure (kPa)
$\chi$	Effective stress parameter
$\psi_o$	Osmotic suction (kPa)
$\psi_m$	Matric suction (kPa)
$\psi_t$	Total soil suction (kPa)

# Abstract

The hydro-mechanical behaviour of partially saturated granular materials is of crucial relevance to many engineering applications, e.g. oil and gas recovery, landslide reinforcement and polluted soil treatment, etc. The major challenges to model the hydro-mechanical behaviour in porous media are the intrinsic complexity of phase distribution and mechanism interplay in the multiphase systems. A wide variety of approaches have been applied to predict the phase distribution and mechanical behaviour of immiscible fluids flow. In this study, we employed a method combining experimental observations and statistical analyses to understand and describe the spatial and temporal information of multiphase flow in porous media.

In this thesis, the distribution of saturated clusters in a granular material is characterised by an optical imaging method in a modified rectangular Hele-Shaw cell under different drainage conditions. A saturated cluster is formed when a liquid phase fully occupies the pore space between solid grains. The formation of these clusters during the liquid withdrawal processes is governed by three competing mechanisms arising from viscous, capillary, and gravitational forces. The net effect of these mechanisms can be varied by tilting the container and employing different flow rates, i.e. varying the drainage conditions on the multiphase system. In this way, the spatial and temporal configurations of saturated clusters in the granular materials are recorded and categorised under various drainage conditions.

We first experimentally evaluated the evolution of the saturated cluster size distribution with respect to the interplay of mechanisms during drainage processes. A morphological image processing method was applied to transform the photos of the rectangular Hele-Shaw cell into a data stream of saturated cluster sizes collected during liquid drainage processes. The saturated cluster size was found to follow a lognormal distribution. It is observed that the scale parameter ( $\mu$ ) and shape parameter ( $\sigma$ ) have negative correlation and positive correlation with the generalised Bond number ( $Bo^*$ ) which considers the complex interplay among viscous, capillary and gravitational forces. This suggests that there is a function containing  $\mu$ ,  $\sigma$  and  $Bo^*$  for describing the cluster distribution at various saturation levels for given drainage conditions.

We further investigated the relation between porous media packing characteristics and the resulting saturated cluster distribution. We considered the crystallisation effect on saturated

cluster distributions by utilising the pore-scale information from the Voronoi and Delaunay tessellation. The results indicated that the distributions of both the crystallised cell size and pore size are positively correlated to the spatial and temporal distribution of saturated cluster sizes. This provided an insight into predicting the phase distribution for multiphase flow using the topological information in an existing porous medium.

To conclude, we developed a fundamental understanding of the formation and evolution of clusters in partially saturated granular materials by investigating multiphase flow in porous media. With further consideration of the total surface energy obtained based on liquid-air interfaces, we were able to include additional grain-scale information in the constitutive modelling of unsaturated soils using both the saturation degree and generalised Bond number,  $Bo^*$ . These findings have successfully bridged the pore-scale behaviours with the overall hydro-mechanical characteristics in partially saturated soils.

# Contents

<b><u>ACKNOWLEDGEMENTS</u></b>	<b><u>III</u></b>
<b><u>NOTATION</u></b>	<b><u>IV</u></b>
<b><u>ABSTRACT</u></b>	<b><u>VI</u></b>
<b><u>CHAPTER 1 INTRODUCTION</u></b>	<b><u>1</u></b>
<b><u>CHAPTER 2 LITERATURE REVIEW</u></b>	<b><u>4</u></b>
<b>2.1 FUNDAMENTAL CONCEPTS</b>	<b>4</b>
2.1.1 SURFACE TENSION, CONTACT ANGLE AND CAPILLARY EFFECTS	4
2.1.2 FOUR REGIMES OF LIQUID CONTENT	7
2.1.3 BOND NUMBER (BO) AND CAPILLARY NUMBER (CA)	8
2.1.4 EFFECTIVE STRESS IN UNSATURATED SOIL	8
<b>2.2 INTERFACE PROPERTIES OF MULTIPHASE FLOW</b>	<b>9</b>
2.2.1 GENERALISED BOND NUMBER (BO*)	9
2.2.2 DRAINAGE FRONT	10
<b>2.3 MECHANICAL PROPERTIES IN MULTIPHASE FLOW</b>	<b>12</b>
<b><u>CHAPTER 3 EXPERIMENTAL METHODS</u></b>	<b><u>15</u></b>
<b>3.1 EXPERIMENTAL DESIGN</b>	<b>16</b>
3.1.1 EXPERIMENTAL SCHEME	16
3.1.2 EXPERIMENTAL EQUIPMENTS	17
3.1.3 MEASUREMENT PROCEDURE	18
<b>3.2 DATA ACQUISITION AND PROCESSING</b>	<b>19</b>
3.2.1 IMAGE PROCESSING METHODS	19
3.2.2 STATISTICAL ANALYSIS METHODS	22
<b>3.3 SUMMARY</b>	<b>25</b>

<b>CHAPTER 4 MATERIAL CHARACTERISATION</b>	<b>26</b>
<hr/>	
<b>4.1 LIQUID</b>	<b>26</b>
4.1 SURFACE TENSION	26
4.1.2 CONTACT ANGLE	28
4.1.3 VISCOSITY	29
<b>4.2 MORPHOLOGICAL ANALYSIS OF GLASS BEADS</b>	<b>31</b>
<b>4.3 PORE NETWORK ANALYSIS</b>	<b>33</b>
4.3.1 VORONOI CELL DISTRIBUTION	33
4.3.2 DELAUNAY TRIANGLE DISTRIBUTION	34
<b>CHAPTER 5 CHARACTERISTICS OF SATURATED CLUSTERS UNDER DIFFERENT DRAINAGE CONDITIONS</b>	<b>36</b>
<hr/>	
<b>5.1 LIQUID FRONT CHARACTERISTICS WITH <math>Bo^*</math></b>	<b>36</b>
<b>5.2 SATURATED CLUSTER SIZE DISTRIBUTION</b>	<b>40</b>
5.2.1 PROBABILITY DENSITY DISTRIBUTION OF SATURATED CLUSTERS	42
5.2.2 MAXIMUM LIKELIHOOD FITTING	45
5.2.3 STATISTICAL DISTRIBUTIONS	48
5.2.4 FUNCTION OF $Bo^*$ AND $\mu/\sigma$	49
<b>5.3 DISCUSSION</b>	<b>50</b>
<b>5.4 SUMMARY</b>	<b>51</b>
<b>CHAPTER 6 PORE-STRUCTURE DEPENDENT SATURATED CLUSTER DISTRIBUTION</b>	<b>53</b>
<hr/>	
<b>6.1 VORONOI AND DELAUNAY TESSELLATION ANALYSIS</b>	<b>54</b>
<b>6.2 EFFECT OF VORONOI/DELAUNAY CELL AREA DISTRIBUTION ON THE WETTED CELL AREA DISTRIBUTION</b>	<b>55</b>
<b>6.3 SPATIAL DISTRIBUTION OF WETTED CELLS</b>	<b>60</b>
<b>6.4 DISCUSSION</b>	<b>61</b>
<b>6.5 SUMMARY</b>	<b>62</b>
<b>CHAPTER 7 CONCLUSION</b>	<b>63</b>
<hr/>	
<b>REFERENCES</b>	<b>65</b>
<hr/>	

<b>APPENDIX A: IMAGE PROCESSING</b>	<b>69</b>
<b>APPENDIX B: MAXIMUM LIKELIHOOD ESTIMATION</b>	<b>71</b>
<b>APPENDIX C: LOGNORMAL PARAMETERS</b>	<b>73</b>
<b>APPENDIX D: WETTED CELL DISTRIBUTION</b>	<b>75</b>

# Chapter 1

## Introduction

Multiphase fluid flows in porous medium have been subjected to a considerable number of studies over the past decades due to its importance in a broad range of applications, including oil recovery, risk assessment of landslides, and groundwater hydrology [6-8]. Strong variations of displacement structure exist in two or more immiscible fluid flows in porous medium, depending on many physical properties of both the involved fluids and porous media. These properties include the flow rates, wetting properties, viscosity ratio and density difference of the involved fluids, and morphological properties of pore structure [9-11]. The formation of drainage fronts (interface between wetting and non-wetting fluids) and displacement dynamics, shaped by the aforementioned properties, determine the residual liquid phase distribution in partially wetted porous media and affect the relative permeability of the correlated unsaturated regions. Recent years, experimental and numerical studies concerning drainage processes in porous media often tend to focus on the evolution of viscous fingering at various flow rates. However, studies on the morphological characteristics of liquid phase entrapment behind the front remain relatively scarce. Accurate predictions of the liquid fractions that can be drained and that are trapped behind the drainage front are essential to quantify the relative permeability and the effective stress of unsaturated soils or rocks [8, 12]. In Fig. 1.1, evidence suggests that in same water content scenarios, the mechanical behaviours of partially wetted porous media are characterised by the distributions of liquid phase in the porous media. In the following discussion, an improved understanding of the entrapment dynamics hinges a better description of drainage front movements.

For low flow rates, the invasion events along the displacement front occur visually, pore by pore which can be predicted by the classic percolation theory. However, for high flow rates, pores are invaded simultaneously, exhibiting large pressure bursts with liquid ejection during the pressure relaxation. This phenomenon is manifested primarily through the complex interplay of three forces within the system, namely gravitational force, viscous force and capillary force. In a drainage process, the viscous force limits flow through narrow pores,

whereas the gravitational force stabilizes and balances the effect of viscous forces. With increasing drainage rates, gravitational force can no longer balance this effect and the non-wetting phase can invade the porous medium from a few locations. The rapidly growing “viscous fingers” contribute to viscous unstable flows in porous media.

This dependency of displacement front morphology on the flow rates raises the following question: how would this affect the fractions of liquid phase entrapped behind a moving drainage front? *Wildenschild et al.* [13] used X-ray tomography to image air invasion into the saturated sandy soil and observed that large values of residual saturations occurred for high flow rates. The same trend was observed in glass bead micromodels in *Løvoll’s* study [14]. The observed increase in residual saturation behind the displacement front is due to the preferential drainage of large pores bypassing and entrapping liquid phase in non-invaded volumes [5]. In addition, the entrapped liquid phase behind rapid moving fronts is not indefinite entrapment. In fact, it drains with a significantly small rate compared to the one of the primary moving front. This redistribution flow and the dominant liquid flow can affect the formation and evolution of the discontinuous entrapped liquid phase.

This study aims to find a link between the complex mechanisms inside the porous media and

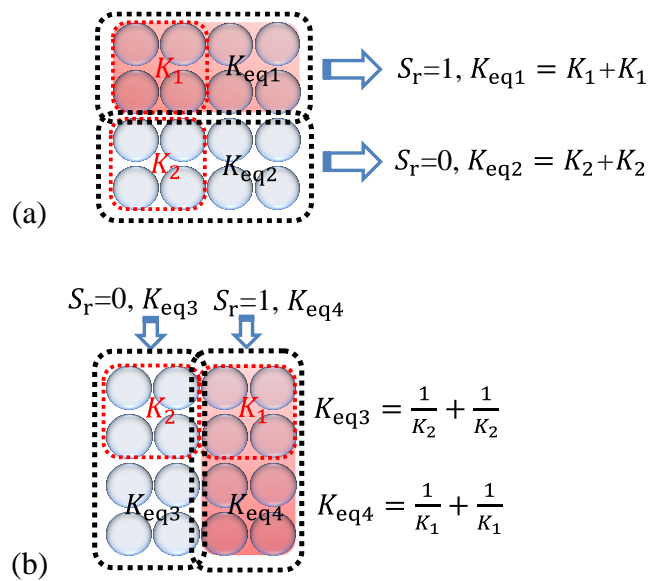


**Fig. 1.1** Comparison of effective stresses of two wetted porous media with same water content (50%).  $K_1$  and  $K_2$  indicate the spring constant for the four adjacent fully saturated or dry solid grains;  $K_{eqi}$  indicates the equivalent spring constant for the adjacent eight fully saturated or dry solid grains.

the morphological characteristics of discontinuous entrapped liquid phase (saturated clusters).

To quantify the magnitudes of viscous or gravitational forces relative to the capillary force, two dimensionless numbers, *i.e.*, the Capillary number (Ca) and Bond number (Bo), are employed in our analysis. The properties of “viscous delayed” region are studied in this thesis by establishing an experimental system where capillary, gravity and viscous forces can be examined. We have studied the saturated clusters obtained by draining water from a porous medium. To tune the gravitational and viscous forces, different tilting angles and drainage rates were employed on the system. The temporal and spatial information of the saturated clusters was characterised by using a digital camera and subsequent image processing. The size distribution of saturated clusters was extracted from a series of images and statistically analysed by employing maximum likelihood estimation. In addition, the effects of pore structure on the onset and spatial extent of liquid phase entrapment were analysed by the mapping the pore network to its corresponding pictures.

This present thesis is organised as follows. In Chapter 2, we present a literature review on a macroscopic theoretical framework for defining the viscous effects on saturation profiles behind the rapid moving fronts. We introduce a dimensionless parameter ( $Bo^*$ ) to mark the onset of unstable flows. The experimental setup and methods for data analyses are described in Chapter 3, for which variations in the forced drainage rates and inclination angles of the container were applied. The entrapped liquid profiles were also illustrated visually during the drainage processes. In Chapter 4, we present the hydraulic properties of liquid and morphological characteristics of solid grains used in our experiments. In Chapter 5, the saturated cluster size distributions under various loading scenarios are presented and discussed. Chapter 6 presents the influence of pore-scale structure on the spatial extent of saturated clusters. Finally, conclusions are presented in Chapter 7.

# Chapter 2

## Literature Review

In this chapter, we will explain some basic concepts widely used in multiphase flow in porous media, in particular wettability and different pore invasion mechanisms. A few previous studies on the displacement of interface between two immiscible fluids in a porous medium will then be summarized. We start by making some general remarks about fundamental concepts in multiphase flow in porous media.

### 2.1 Fundamental concepts

#### 2.1.1 Surface tension, contact angle and capillary effects

During recent centuries, many phenomena share a unifying feature of being something that happens whenever two or more immiscible fluids are situated adjacent to each other [15]. They all have an interface lying between and separating them apart. It is well known, and it results immediately from the composition of forces, that where a line is equably distended, the force that it exerts, in a direction perpendicular to its own, is directed as its curvature [16]. This interfacial force has a tendency on the surface which makes it acquires the least surface area possible, also called surface tension.

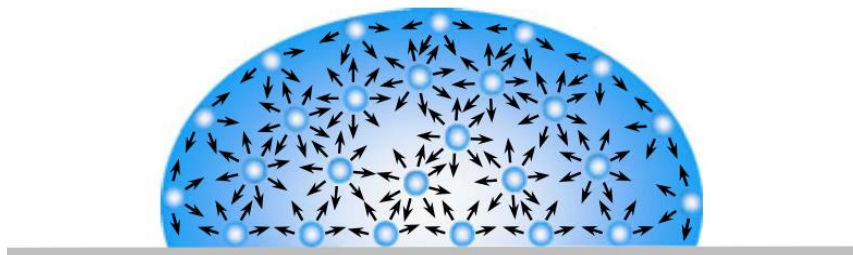


**Fig 2.1** Surface tension is caused by unbalanced forces of liquid molecules at the surface [3].

Ideally, the shape of a liquid droplet on a smooth homogeneous solid surface is determined by surface tension (see Fig 2.1). In a pure liquid, each molecule in the bulk is pulled equally in every direction by neighbouring liquid molecules, resulting in a net force of zero. However,

the molecules exposed at the surface do not have neighbouring molecules in all directions to provide a balanced net force. Instead, they are pulled inward by the neighbouring molecules, creating an internal pressure, which gives the surface area a minimum value. It can be measured using pendant drop method on a goniometer (more details can be seen in Chapter 4).

Surface tension is an important factor in the phenomenon of capillarity, which happens as a liquid flows in narrow spaces without assistance. In physics, the mathematical behaviour of a curved interface between two different phases with interface stress effects can be described by the generalized Young-Laplace equation [16-18]:

$$\Delta p = 2\gamma H, \quad (2.1)$$

where  $\Delta p$  is the pressure difference across the fluid interface and  $\gamma$  is the surface tension,  $H$  is the mean curvature.

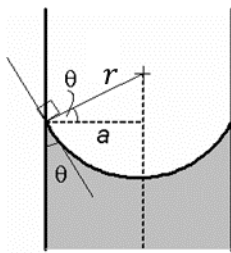


**Fig. 2.2** A capillary tube

Fig. 2.2 shows a capillary tube. In a vertical tube the net attractive forces are symmetrically horizontal, which cause the vertical rise. Molecules being pulled toward the walls force other molecules aside in all directions, resulting in a spread along the walls that is only partly compensated by gravity. When liquid is forced upward along the walls and cohesive forces carry the remaining liquid column with it, a concave meniscus forms. In Fig.

2.2,  $r$  is the radius of the curvature,  $a$  is the radius of the narrow tube and  $\theta$  is the contact angle.

To describe the complex network topology of porous media, we can simplify the narrow space between every two closest solid beads as a capillary tube. In that case, the structure of a porous medium can be interpreted as a combination of thousands of capillary tubes with different diameters. The diameter of each capillary tube is determined by the localised packing characteristics. To have a better understanding of this issue, we need to quantify the capillary tube's size distribution as well as know viscous effects during drainage from a pair of hydraulically coupled capillaries [19, 20].

In two adjacent capillaries with different diameters, water is fully filled initially. A constant withdrawal flow rate  $q_0$  is set at the bottom of the system, shown as the inset picture in Fig. 2.3(a). As the drainage begins, the curvature of meniscus increase and the large capillary first reaches its air entry pressure head. Air enters into a large capillary and the meniscus in the large

capillary starts to recede, while the meniscus in the small capillary stays pinned at the top [21], which can be well explained by Young-Laplace equation [Eq. (2.1)].

Fig. 2.3 describes the temporal evolution of characteristic length  $L_C$  (divided by  $L_G$ , which is maximum capillary pressure head difference balanced by gravity in two neighbouring capillary tubes) in a system of a coupled pair of capillaries with radii  $r_1$  and  $r_2$  of 160 and 80  $\mu\text{m}$  respectively (with  $K_1 = 31.3 \text{ mm/s}$  and  $K_2 = 7.8 \text{ mm/s}$  and  $L_G$  of 92 mm), when viscous force can be neglected [5]. In Fig. 2.3,  $K$  is the hydraulic conductivity of a cylindrical capillary of radius  $r$ :

$$K = \frac{r^2 \rho g}{8\mu}. \quad (2.2)$$

The characteristic length  $L_C$  is related to the meniscus positions for both large and small capillaries  $z_i$ :

$$L_C = z_1 - z_2. \quad (2.3)$$

In the case  $q_0 < K_2$ ,  $L_C$  increases linearly and soon attains a constant value; while in the case  $q_0 > K_2$ ,  $L_C$  continuous to increase while the growth rate decreases as a function of time. The dynamic capillary head difference  $L_C$  between two menisci in neighbouring cylindrical tubes can explain the geometry of drainage front from microscale.

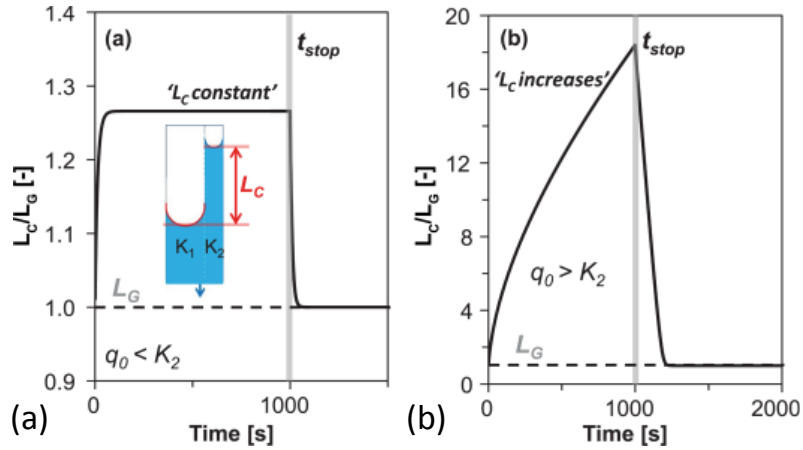


**Fig.2.3** Characteristic length  $L_C$  of a coupled pair capillaries with radii  $r_1$  and  $r_2$  of 160 and 80  $\mu\text{m}$  respectively, drainage rate is  $q_0$  from to  $[L_C(0) = L_G]$  to  $t_{\text{stop}}$ . (a) The case  $q_0 < K_2$ ,  $L_C$  increases linearly and soon attains a constant value. (b) The case  $q_0 > K_2$ ,  $L_C$  continuous to increase while the growth rate decreases as a function of time [5].

To estimate characteristic length  $L_C$  in capillary tubes, we employed the diameter of a capillary tube, which can be interpreted as pore throats in porous medium, to our following analysis. The pore throat, namely the distance between two closest glass beads while excluding the radius of each of the beads from the vector, is the tube diameter. The inverse of pore throat size distribution directly illustrates the capillary pressure threshold distribution in our pore network [22]. The pore throat size distribution of our porous medium is shown in Chapter 4.

### 2.1.2 Four regimes of liquid content

It is well known that apparent cohesion in wet granular materials depends on the amount of liquid in the system [23]. Due to water molecules are highly attracted to the surface of solid phase, there is a thin film of liquid coating on the surface on solid skeleton, shown in Fig. 2.4(a). In many practical problems, this layer of liquid is always considered immobile because it is tightly bonded to the solid surfaces. As the water volume increases, the water tends to fill the acute corners of the pores to minimize the water-air interface area. This is known as the pendular regime, shown in Fig. 2.4(b). Pendular water is less tightly bonded by the solid phase but it still occurs in isolated regions and there is no continuous flow paths. As more water is added to the system, continuous thicker films are formed along the pore walls and it is possible for liquid to flow in this regime. This state is known as funicular regime. In the aforementioned three regimes, air phase is continuous along the central part of the pores. As the volume of water in the system increase further, the fully saturated regime is formed, shown in Fig. 2.4(d). At this stage, water occupies all the pore spaces in the localised region and no trapped air bubbles.

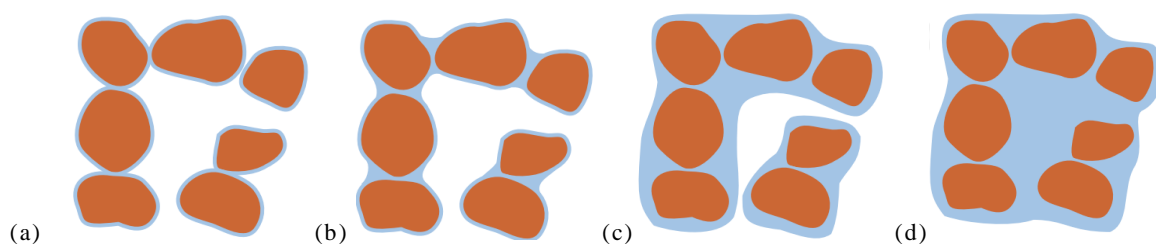


**Fig 2.4** Spatial water-air configuration in unsaturated granular materials: (a) adsorbed regime, (b) pendular regime, (c) funicular regime and (d) fully saturated regime [1].

In our experiments, these four water-air configurations can be observed in an individual picture, and their temporal and spatial information can be transformed into the projection of saturated clusters, more details can be found in Chapter 5 and 6.

### 2.1.3 Bond number (Bo) and Capillary number (Ca)

When one fluid tries to invade another fluid, the difference in their densities and flow directions would denote the influences of gravity forces on the liquid front. The influence of gravity on the displacement structure depends both on the magnitudes of viscous and capillary forces and on gravity components [24-28].

To quantify magnitudes of viscous or gravitational forces relative to capillary force in the following experiments and analyses, we employed dimensionless Capillary (Ca) and Bond (Bo) numbers which are defined as follows [4, 29]:

$$\text{Bo} = \frac{\rho g' a^2}{\gamma} \quad (2.4)$$

$$\text{Ca} = \frac{\mu v a^2}{\gamma k}, \quad (2.5)$$

with the wetting liquid density ( $\rho$ ), the component of gravitational acceleration ( $g'$ ), typical pore size ( $a$ ) assumed to be 1/3 of bead diameter (more details can be found in [30]), viscosity of the wetting fluid ( $\mu$ ), surface tension ( $\gamma$ ), the mean front velocity ( $v$ ), permeability of the medium ( $k$ ). Capillary number describes the ratio of viscous to capillary forces; while Bond number indicates the ratio of gravitational to capillary forces.

### 2.1.4 Effective stress in unsaturated soil

In unsaturated soil mechanics, the degree of saturation ( $S_r$ ) is defined as

$$S_r = \frac{V_W}{V_V}, \quad (2.6)$$

where  $V_W$  and  $V_V$  are the total volumes of water and voids, respectively. The term volume of voids refer to that portion of volume of the soil not occupied by mineral grains [31]. Thus, the degree of saturation is the ratio of the volume of liquid to the volume of voids in the partially saturated porous medium. The degree of saturation is a significant index property, especially with respect to small size porous media. Of even greater importance, however, is the state of liquid in the void of porous medium.

In order to quantitatively assess the behaviour of soil in different saturation levels, a large number of effective stress formulations involving scaling functions have been proposed attributed to Bishop's equation. The classic Bishop's effective stress equation is [2]:

$$\sigma' = (\sigma - u_a) + \chi(u_a - u_w), \quad (2.7)$$

where  $\sigma'$  is the effective interparticle stress,  $\sigma$  is total stress,  $u_a$  is pore air pressure,  $u_w$  is pore water pressure, the quantity  $u_a - u_w$  is defined as matric suction, and  $\chi$  is the effective stress coefficient, a material property that depends on the degree of saturation or matric suction [32-35]. The variation in  $\chi$  between zero and one for perfectly dry and saturated conditions, respectively. However, many researchers have done numerous studies on both experimental and numerical analyses proved that it is not accurate enough to interpret the effective stress as Eq. (2.7) especially at low saturation levels [2, 32, 36]. Another stream has been produced for a more accurate solution.

Unlike in saturated soil, the stress state in unsaturated soil is comprised of the combined contribution from three phases: gas, liquid and solid. The relative amounts and corresponding pressures of the pore water and pore air phases in unsaturated soil have a direct impact on the stress state acting at the particle-particle contacts and, consequently, on the macroscopic physical behaviour of the soil mass [34]. Many researchers have looked deeply into the stress of the liquid (pore water stress) in the void of the porous media, which may be either positive or negative with respect to the atmospheric pressure [2, 35, 37, 38]. The pore water stress is fundamentally related to the behaviour of soil in the field conditions especially at the low saturations. Besides, the liquid cluster distribution characteristics also have a significance influence on the effective stress of unsaturated soil because it determines the interfacial area between different phases in porous media, more details can be seen in Section 2.3.

## **2.2 Interface properties of multiphase flow**

### **2.2.1 Generalised Bond number ( $Bo^*$ )**

Many researchers have done various experimental and numerical studies on fluid displacement in porous media. Different theoretical approaches have been applied to explain the phenomenon of fluid front morphologies ranging from stable liquid front and viscous fingering, including the a coupled pair of capillaries model (mentioned in Section 2.1.1), scaling law for sliding drops [10] and sliding liquid elements within simple geometry model [11]. Based on these models and Auradou's theory [9], Meheust et al. [4] have investigated experimentally the competition between viscous, capillary, and gravitational forces during drainage in a two-dimensional synthetic porous medium, shown in Fig. 2.5. In their study, they introduced a

dimensionless number, generalised Bond number ( $Bo^*$ ), which quantifies the three forces mentioned before.

The generalised Bond number is defined as [4, 19]:

$$Bo^* = Bo - Ca. \quad (2.8)$$

### 2.2.2 Drainage front

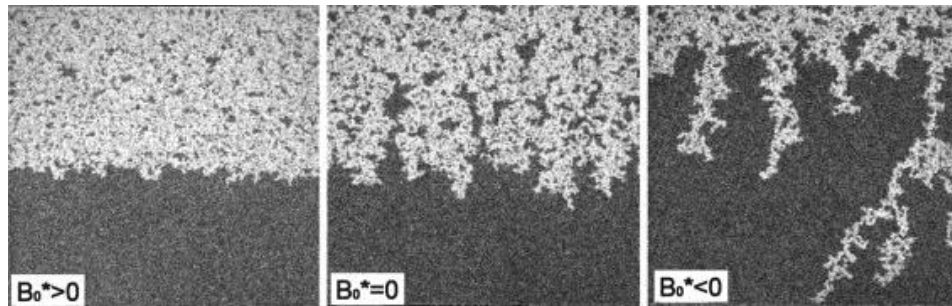


**Fig. 2.5** Experimental results depicting drainage front morphology when air invades into an initially fully saturated Hele-Shaw cell with different generalised Bond numbers ( $Bo^*$ ) [4].

The value of generalized Bond number ( $Bo^*$ ), plays an important role in the resulting front morphology as show in Fig. 2.5. For values of  $Bo^* > 0$  (i.e.,  $Bo > Ca$ ), during drainage, the gravitational force will overcome the viscous effects and lead to a flat plateau of the liquid front. However, for values of  $Bo^* < 0$  (i.e.,  $Bo < Ca$ ), with the diminishing stabilizing force of gravity the front becomes progressively unstable in Fig. 2.5. In other words, it is found that the transition from stable to unstable conditions occurs at  $Bo^* = 0$ . [39-43]. To reveal the influence of generalized Bond number on the morphological characteristics of liquid front, two methods are introduced here, namely maximal extension and fractal dimension of the liquid front.

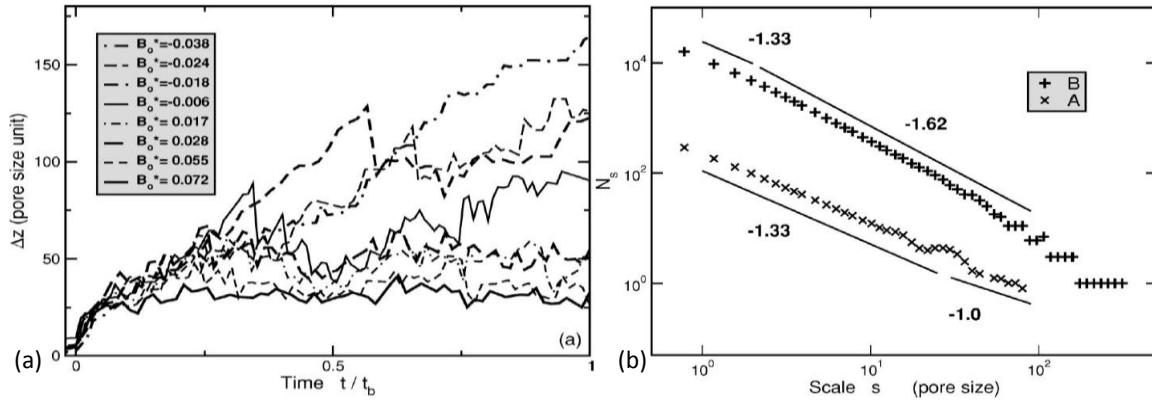


**Fig. 2.6** (a) Evolution of the extension of the front along the direction of displacement ( $z$ ),  $\Delta z$  as a function of time normalized by the time at breakthrough. (b) The relationship between the number of the boxes covering the edge of the figure and scale size of two fronts (labeled A and B) from two individual experiments with no gravity. Front A corresponds to an experiment with extremely low withdrawal rate, 0.006ml/min; while front B corresponds to an experiment with a withdrawal rate of 5ml/min.  $N_s$  is the number of boxes of side length  $s$  required for entirely covering the front [4].

Firstly, the maximal extension of liquid front along the drainage direction  $\Delta z$ , is a widely used variable to quantify the characteristics of liquid front. It is defined as the maximal vertical distance between two points on the front. The small and constant  $\Delta z$  values shows the relatively flat liquid morphology; while the large  $\Delta z$  values illustrate the relatively fluctuate liquid front morphology. Fig. 2.6(a) appears the destabilization of liquid front for both positive and negative  $Bo^*$  values as a function of time normalized by the time at breakthrough. At large positive  $Bo^*$  values, the front extension  $\Delta z$  quickly grows to a small constant value while as the generalized Bond number decreases, it shows big fluctuations of  $\Delta z$ . The sudden drop of  $\Delta z$  shown in Fig.2.6(a) represents the merging of two nearby fingers, which occurs as the generalized Bond number has negative values. When generalized Bond number has positive values, the sudden drop disappears as a small number of viscous fingers exist, which never merge.

Compared with two-point correlation method, fractal dimension is another widely used factor which describes the geometry characteristics of whole liquid front [44]. The basic principle to estimate fractal dimension  $D$  is based on the concept of self-similarity. The fractal dimension is an index for characterizing the space filling ability of fractal patterns. The larger the index value of the pattern, the stronger space filling ability it has. The fractal dimension for a curve

has the value between one and two, which can be simply illustrated as when the index is close to one the morphology of the curve is close to a flat plateau; while when the index is close to two the morphology of the curve is more fluctuated. To estimate the value of fractal dimension, box counting method was used by Meheust et al. [4] in 2002. The linear regression to estimate fractal dimension is generally defined as the following equation [45-48]:

$$D = \lim_{s \rightarrow 0} \frac{\log(N_s)}{\log(1/s)} \quad (2.9)$$

By counting the number of boxes covering the sides of the figure and do the same thing by using a finer grid, box-counting method is a method of gathering data for analysing complex patterns by breaking an object into smaller and smaller pieces, typically "box"-shaped, and analysing the pieces at each smaller scale [47-53]. In this method, each image is covered by a sequence of grids of descending sizes and for each of the grids, two values are recorded: the number of square boxes interested by the image ( $N_s$ ), and the side length of the squares ( $s$ ). A plot Fig. 2.6(b) shows the relation between  $N_s$  and  $s$ . The slope of the line is the fractal dimension of the object [47]. Fig. 2.6(b) shows that labeled A and B lines representing capillary and viscous fronts respectively. The front labeled A corresponds to the overall front of an experiment with a very slow withdraw rate 0.006ml/min and the front labeled B corresponds to a sole front of an experiment with no gravity force and a withdraw rate 5ml/min, i.e.,  $Bo^*(B) < Bo^*(A)$ . The fractal dimensions for family A and family B are close to 1.3 and 1.6, respectively. Fig. 2.6(b) shows for negative generalized Bond numbers, fronts with larger absolute value have larger fractal dimension, i.e. the fronts are more fluctuated.

## 2.3 Mechanical properties in multiphase flow

The total soil suction quantifies thermodynamic potential of soil pore water relative to a reference potential of free water, which regards to water containing no dissolved solutes, having no interactions with other phases that impact curvature to the air-water interface, and having no external forces other than gravity [34]. The total soil suction is mainly formed with three physical and physicochemical mechanisms, including capillary effects, short-range adsorption effects and osmotic effects. The former two are usually grouped with a more general term in unsaturated soil mechanics as matric suction.

In granular media, capillary effects include the curvature of air-water interface and the adsorption between two closest solid beads in a three-phase soil-water system. Short-range

adsorption effects arise from electrical and van der Waals force occurring within the solid-water interface. Osmotic effects are the result of dissolved solutes in the pore water.

Suction arises from combined effects of capillary and short-range adsorption is referred to as matric suction  $\psi_m$ . Suction arises from osmotic effects is referred to as osmotic suction  $\psi_o$ . Thus, the total soil suction,  $\psi_t$ , can be interpreted as:

$$\psi_t = \psi_m + \psi_o. \quad (2.10)$$

At different saturation levels, the total soil water suction is dominated by different mechanisms. At low saturation levels, the liquid in the porous medium is mostly in the form of thin film liquid coating on solid grains. The dominant mechanism is the short-range adsorption effects attributed by the surface properties of the soil solids, leading to a relatively high suction stress. At high saturation levels, the liquid trapped in pore structure is mostly in the form as connected or disconnected liquid clusters in the pore pockets. In this case, the capillary effects become the dominant mechanism for high saturation levels. The particle and pore structure and pore size distribution are the main factors determine the capillary effects [54].

To best illustrate the relationship between water content and suction stress, the soil-water characteristic curve, SWCC, is introduced. The morphological characteristics of SWCC reflects the material properties of various soil, including the density, pore size distribution, grain size distribution and clay content, shown in Fig. 2.7. Likos (2014) [2] took the surface tension and interfacial area of different phases in a multiphase system into account. Four experiments were done on different types of soils: F-75 Ottawa sand, river sand, concrete sand and Texas sand. The median grain sizes of four types of soil shown in Fig. 2.7 increase from 0.2mm to 1.24mm.

The solid lines are the initial drying curves and the dashed lines are the initial wetting curves. Among all four figures, the interfacial area has the largest value at relatively lower saturation level during wetting processes. Results have shown that the contribution of interfacial forces to effective stress in unsaturated soil can be very significant at low saturation levels and wetting processes. The difference for suction stress with and without accounting for the interfacial forces can be up to 140% at  $S_r=0.1$  in wetting processes. In this case, the neglecting of interfacial forces in computing effective stress at some circumstances appear to be inaccurate for practical problems. Thus, it is important to build a relation between the interfacial area and effective.

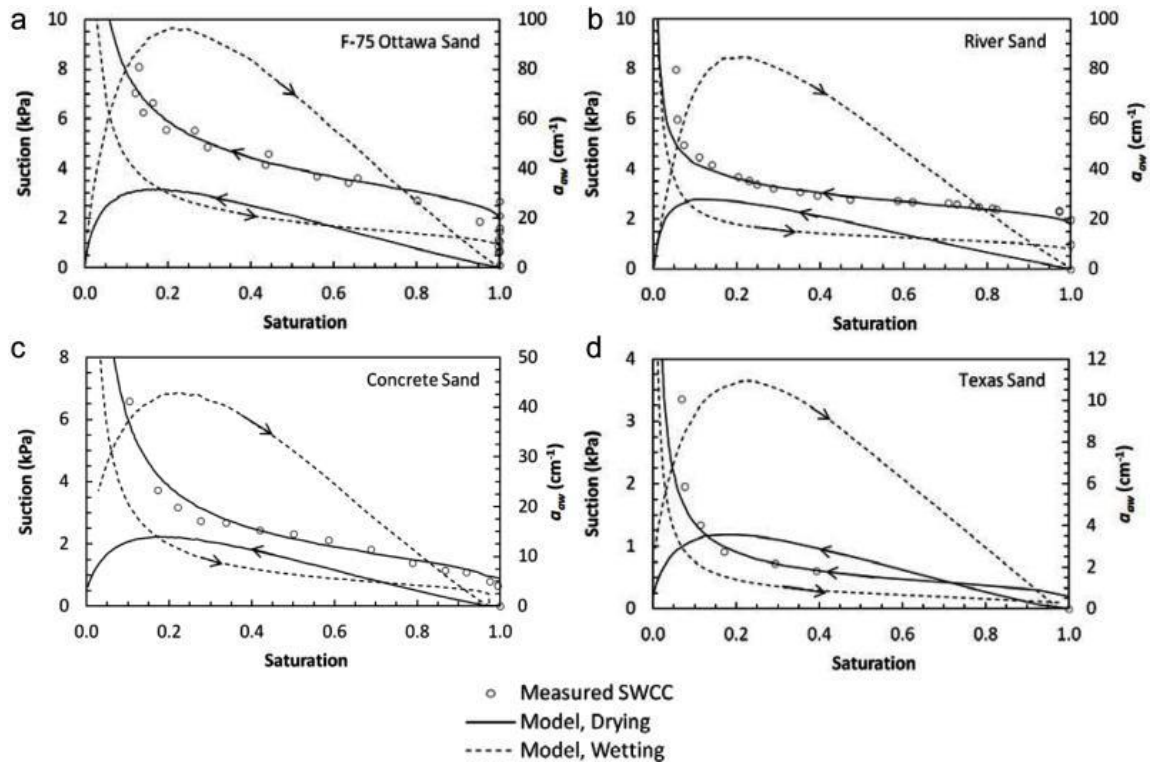


**Fig. 2.7** Measured and predicted water retention curves and air-water interfacial area for four types of soil: (a) F-75 Ottawa sand; (b) river sand; (c) concert sand; and (d) Texas sand [2].

# Chapter 3

## Experimental Methods

As mentioned in the introduction, understanding the role of coefficient ( $\chi$ ) of effective stress on the degree of saturation has always been a challenging task for both experimental and theoretical perspectives. Many researchers have conducted the experiments about the dynamic behaviour of drainage fronts in porous media [4, 14, 19, 55-58]. In 3D systems the visualisation of flow profile is still challenging [59], even with transparent media; however, in quasi-2D systems, the immediate visualization of flow structure is simpler and it is easy to access by a digital camera. The aim of our research is to systematically observe the saturated clusters behind its drying front in a modified Hele-Shaw cell when the water is drained from one side of the container.

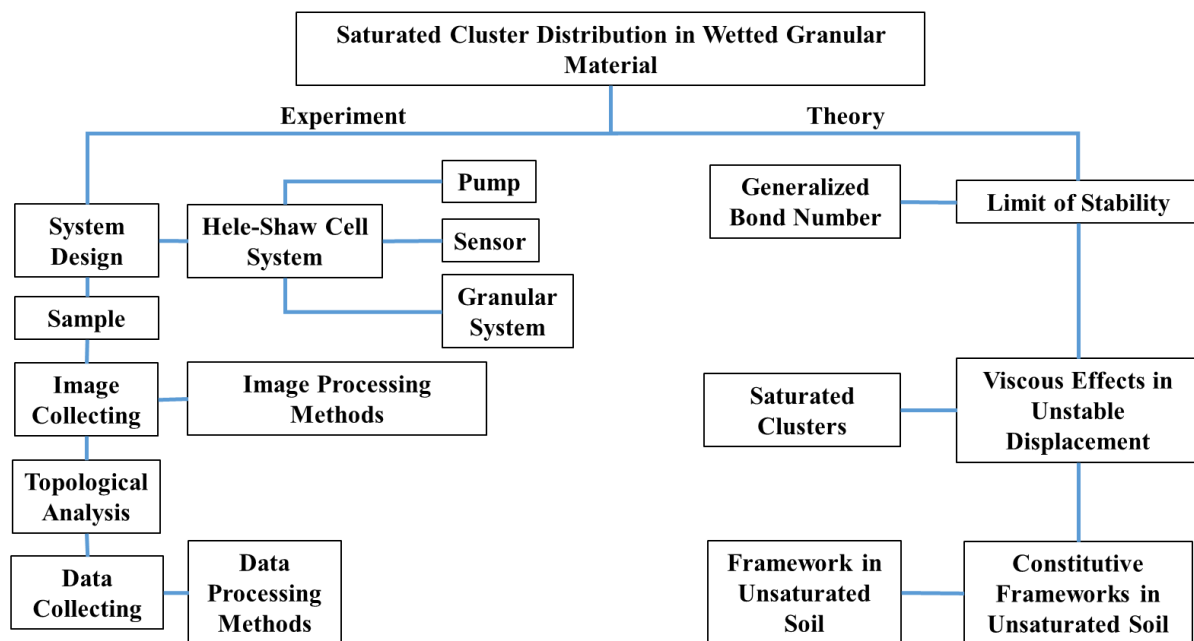


Figure 3.1 Flow chart of the project

Fig. 3.1 shows the flow chart of our project which can be divided into two parts: experiment and theory. In the experimental system, a modified Hele-Shaw cell filled with a monolayer of glass beads formed the porous medium. By employing a different generalized Bond number,

which quantifies the magnitudes of viscous and gravitational forces to the capillary force, various flow features can be generated. Data is extracted from images taken from the top by a digital camera using topological analysis and statistical methods.

The general methods employed in this experimental investigation are explained in this chapter. Also, an overview of the experimental design is given and data acquisition and processing methods are explained. Then, the image analysis techniques and data analysis methods are exemplified. Finally, a summary of the methodology is given.

### 3.1 Experimental design

#### 3.1.1 Experimental scheme

To investigate the characteristics of saturated cluster distribution behind its drying front, a series of drainage experiments was performed with a variety of tilt angles as well as drainage rates. The applied flow rates ranged from 1 ml/min to 20 ml/min for different tilt angles. These resulted in various mean front velocities, which were determined from volumetric flow rates at

**Table 3.1.** Evaluative parameters mean front velocity and generalized Bond number ( $Bo^*$ ) are given.

Tilt Angle (°)	0					
Drainage Rate (ml/min)	1	2	5	10	20	
Mean Front Velocity (mm/s)	0.116	0.231	0.579	1.157	2.315	
$Bo^*$ (-)	$-1.556 \times 10^{-4}$	$-3.111 \times 10^{-4}$	$-7.778 \times 10^{-4}$	-0.002	-0.003	
Tilt Angle (°)	5		10		15	
Drainage Rate (mL/min)	1	5	20	5	20	10
Mean Front Velocity (mm/s)	0.116	0.579	2.315	0.579	2.315	1.157
$Bo^*$ (-)	0.006	0.005	0.003	0.010	0.009	0.016

the cross-section area taking into account the porosity (shown in Table. 3.1). As a result, both stable and unstable drainage front morphologies were observable in our experiments.

It is noted that temperature may affect the resulting capillary force, therefore, the temperature should be strictly controlled during the test. The laboratory temperature was controlled at 24-25°C.

### 3.1.2 Experimental equipments

The experimental system was designed for temporally and spatially resolved imaging of interface motions in micro-models consisting of glass beads. The key elements of the experimental setup are shown in Fig. 3.2(a). A two-dimensional porous medium was constructed by a single layer of glass beads with a diameter of 2 mm between two parallel glass plates. The glass plates and beads were then slightly compressed by a few clamps, and silicone glue was applied on the bottom and side edges, leaving the top side in contact to the atmosphere. The observable area was 180 mm×270 mm, and the resulting porosity was about  $n \approx 0.4$ . After the model was installed, the outlet channel was connected to a dispensing pump (Masterflex 77200-62, USA) that controlled a stable volumetric injection and withdrawal flow rate. A digital camera (Nikon D3300) controlled by a computer over digiCamControl software was used to record the experiments at given time eclipses based on different flow rates. Each image was rescaled with 1000×1500 pixels, which corresponds to a spatial resolution of 30 pixels per mm<sup>2</sup>. An electroluminescent panel provided sufficient background illumination for different shutter speeds. Both the light source and modified Hele-Shaw cell model could be tilted spontaneously to various inclination angles to vary the gravitational component on the fluid flows in the porous medium. The component of gravity along the model  $g'$  is given by  $g \sin(\alpha)$ , where  $g$  is the gravitational acceleration and  $\alpha$  is the inclination angle.

Water was used as the wetting fluid, dyed with dye tracer (Cole-Parmer 00298-06), and air was the non-wetting fluid invading from the open top edge. Experimental values of the wetting fluid were calculated by assuming room temperature at 25°C. The surface tension between two fluids  $\gamma$  was measured with pendant drop method and the wetting fluid viscosity  $\mu$  was measured with rheometer, more details can be found in Chapter 4. The density  $\rho$  of the dyed liquid is 998 kg/m<sup>3</sup>. The permeability of the medium  $k$  was estimated from the Kozeny-Carman relation as  $4.89 \times 10^{-9} \text{ m}^2$  [60].

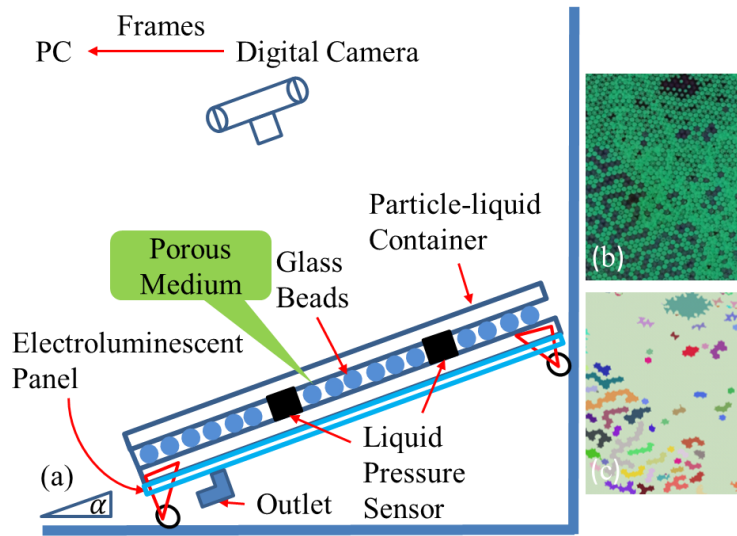


**Figure. 3.2** Diagram of the experimental setup. (a) The camera, electroluminescent panel and cell are all connected to a common frame that can be tilted by an angle. The liquid outlet on the bottom is connected to a syringe pump that injects and withdraws the liquid. (b) A detailed zoom-in section from the raw image extracted from the camera showing the structure of the porous network, the non-wetting phase (green) and wetting phase (red). (c) The same section after applying image processing. Individual saturated clusters are coloured randomly to allow the visualisation of separated clusters for different sizes.

### 3.1.3 Measurement procedure

Fig. 3.3 shows the flow chart of the experimental system. The pump injects and withdraws liquid with a stable volumetric liquid flow rate to or from the container. The inset subfigure in Fig. 3.3(a) shows the liquid saturation calculated from the pump in comparison to the liquid saturation obtained from image-based processing for the entire experimental region for the drainage-injection cycles with different Capillary numbers,  $Ca$ . The electronic pressure sensors records the liquid pressure during injection-drainage cycles and images were collected by a digital camera that was always sitting above the liquid phase. Fig 3.3(b) shows the spatial-temporal evolution of a drainage experiment. The interface between two phases shrink from the top of the container to the bottom, leaving saturated clusters behind the liquid front. After employing a series of image processing methods (see Section 3.2.1), further data regarding to each image can be extracted.

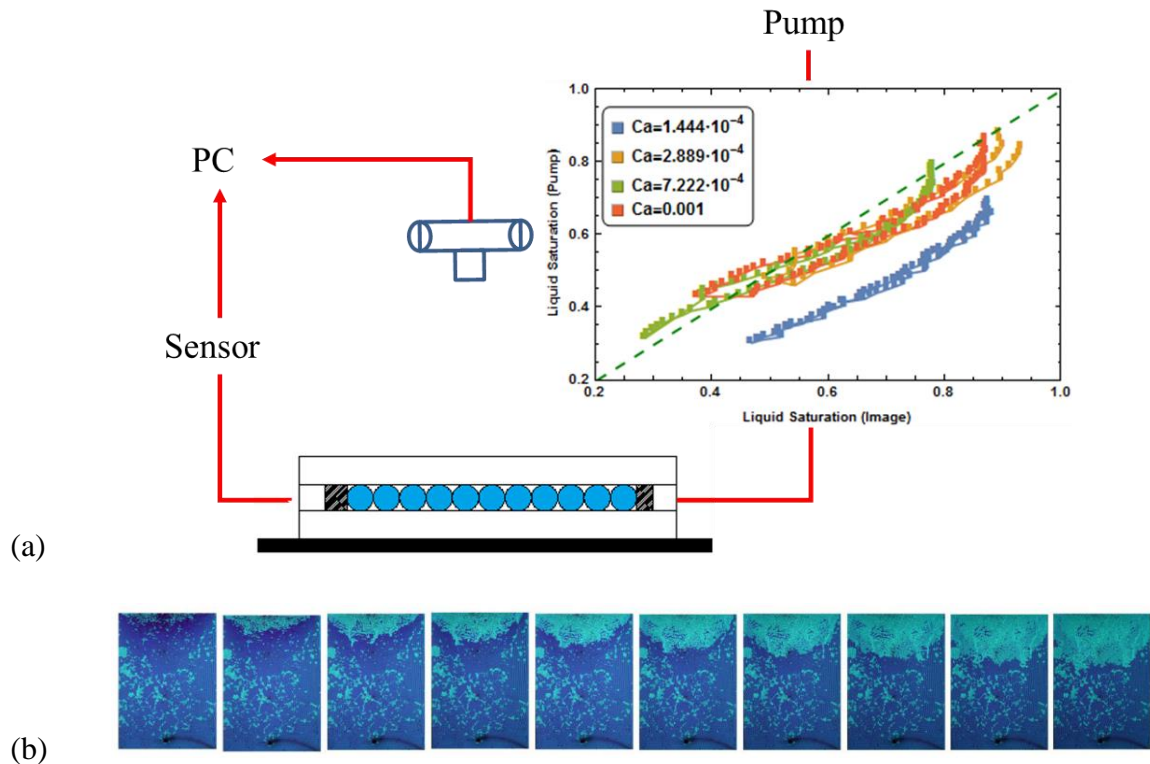


**Figure. 3.3** (a) Flow chart of the experiment system. (b) Experimental images of spatiotemporal evolution of the drainage process for the same drainage rate.

## 3.2 Data acquisition and processing

### 3.2.1 Image processing methods

Once the experimental data is recorded, the next step is to perform the analysis. In particular, we need to extract relevant information from a vast amount of pictures with image analysis techniques. Each run produced more than 60 high-resolution images taken with a 24 megapixels Nikon D3300 camera. Image processing was performed with Mathematica image processing toolbox that has many high-level functions to accomplish complex objectives, allowing for more productive image processing capabilities (Appendix A).

The first step in image analysis is to binarise the images in order to extract the growing saturated clusters. RGB images are extracted from digital camera located right above the cell and converted into greyscale by eliminating the hue and saturation information while retaining the luminance. Fig. 3.5 shows a histogram of the pixel levels for each channel in different images. In grayscale image, the pixel intensity is expressed within a given range between a minimum and a maximum, inclusive. This range is represented in an abstract way as a range from 0 (total absence, black) and 1 (total presence, white), with any fractional values in between. Regions with light grey shadings (higher pixel intensity levels) correspond to air and others with dark shadings (lower pixel intensity levels) correspond to dyed water [shown in Fig. 3.4(a)]. The inner rings in each solid beads are shown in Fig. 3.4(d). Small amount of water is trapped between the void space between glass beads and front and back glass plates. Based on the micromodel geometry, the pore space in our sample can be illustrated in two ways: a 3-D sphere network and a 2-D cylinder network. These rings are discarded in both representations [19].

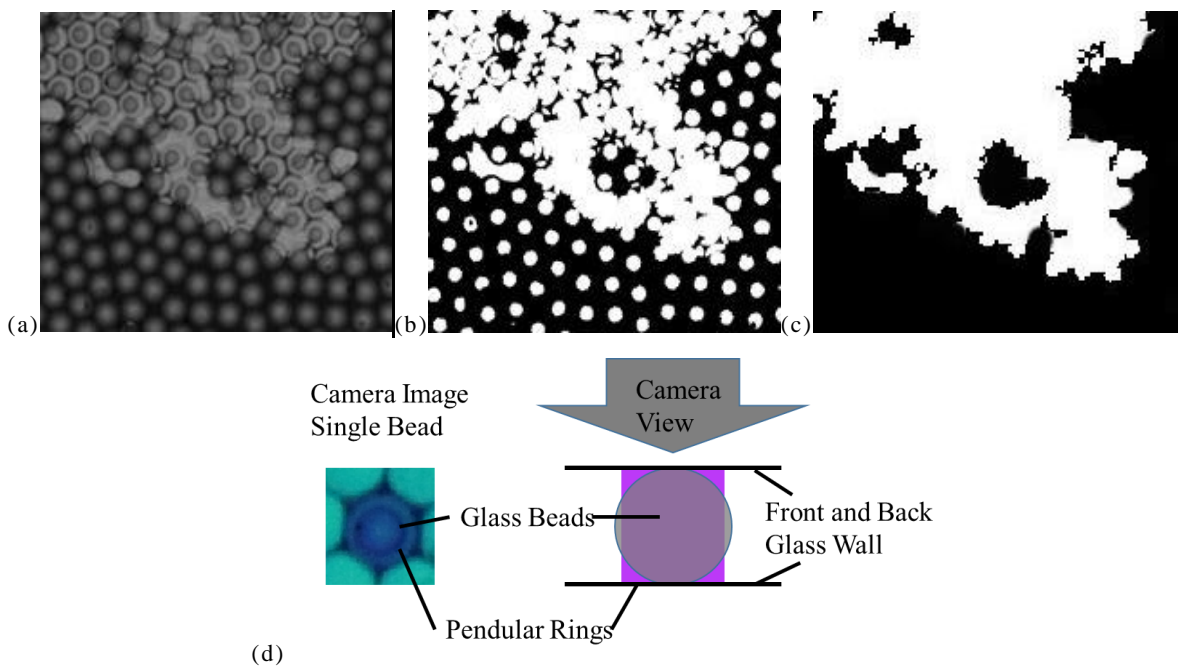


**Fig. 3.4** Comparison between greyscale and binary images. The withdrawal rate is 5 ml/min. The inclination angle is  $10^\circ$ . (a) Greyscale image. (b) Corresponding extracted black and white image. (c) Black and white image after removal of small components with area smaller than  $\pi \text{ mm}^2$ . (d) Top view of pendular rings between the glass bead and the front glass wall and cross-section schematic of a glass bead and pendular rings .

The grayscale pixel-intensity histogram has two distinguishable peaks (shown in Fig. 3.5) corresponding to the non-wetting and wetting phases. In order to separate the air-filled region from the saturated region, all grey levels under a given threshold were set to black ('wet') while the others were white ('dry') [shown in Fig. 3.4(b)]. Threshold values were set to the local minimum values of the grey level histogram and varied from images to images to account for the frequency changes of the electroluminescent panel. After the thresholding process, the whole observation area was separated into different regions with glass beads determined to be part of wet or dry region. This treatment did not affect the following analyses since only the saturated regions that were larger than a projection area of a typical glass bead ( $\pi \text{ mm}^2$  in this study) were considered [shown in Fig. 3.4(c)]. This was achieved by deleting small components with area less than  $\pi \text{ mm}^2$  while color negating the full image for two times. After removal of trapped liquid volume with the projection area smaller than a single glass bead, the resulting black and white picture could provide the required geometrical information. To allow visualising separate clusters of different sizes, analyses of morphological components and watershed separation method have been carried out and colours were assigned to localised saturated clusters [shown in Fig. 3.2(b) and (c)].

According to Fig. 3.2(b), some locally crystallised regions can be seen from our micromodel. Since the porous medium is randomly distributed, crystallization cannot be avoid. In order to investigate their effects on our further statistical analysis and be more precise about what is understood as a pore and a pore-throat, two important graphs associated with the network were generated: Voronoi tessellation and Delaunay triangulation. We begin by finding the centroids of all glass beads in the sample. The Voronoi cells and Delaunay triangles are defined over

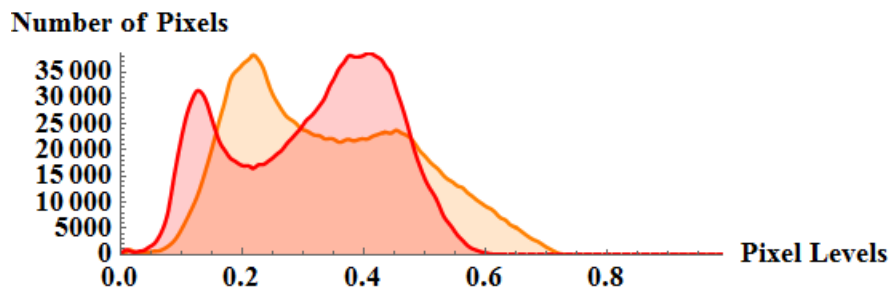


**Fig.3.5** The density distribution of pixel intensity for greyscale photos with  $S_r = 0.7$  (orange) and  $S_r = 0.5$  (red).

these sets of points. Fig. 3.6 indicates the analysis, with two graphs overlaid on top of raw binary image.

In Fig. 3.6, the pore throats can be formally seen as the part of each Delaunay link between two neighbouring glass beads. The void area is defined as the region area of each Voronoi cell excluding the bead. The Delaunay pore area is interpreted as the area of each Delaunay triangle between every three neighbouring glass beads excluding half projection area of an individual glass bead.

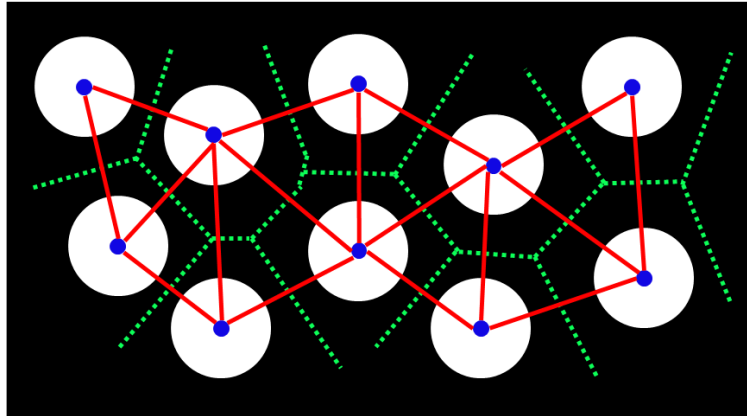


**Fig. 3.6** Graphs correlated to the pore-space structure. The blue dots indicate the centres of glass beads, green dashed lines are the Voronoi tessellation and red solid lines indicate Delaunay triangulation. A Voronoi cell is understood as the region inside each Voronoi polygon including the glass bead. The centres of pore throats are associated to the intersections of Voronoi cell boundaries and Delaunay links.

Once the pore networks are generated, we can measure many important quantities. For example, by using these graphs in connection to the drainage images with different saturation levels, we were able to find the correlation between the wetted cell (inside saturated clusters) distribution and void area, as well as Delaunay pore area. We will discuss these correlations in Chapter 6.

### 3.2.2 Statistical analysis methods

In statistics, the goal of data analysis is to identify the population which is most likely to generate the sample. Each population is identified by a corresponding probability distribution. A unique value is associated with each population as the model parameter, which defines the shape of the distribution profile. In this paper,  $f(y|w)$  denotes the probability density function specifying the observing data vector  $y$  given the parameter  $w$ . Throughout this thesis, the

subscript letter for the vector element  $y$  denotes statistically independent observations. Then according to the theory of probability, the PDF for  $y = (y_1 \dots y_m)$  can be expressed as a multiplication of PDFs for them. Based on the saturated clusters distribution curves in Section 5.2.1, lognormal distribution is selected to best represent our results.

The probability density function of lognormal distribution, taken on two parameters, describes the relative likelihood for the continuous random variable to take on a given value is [61]

$$f(X|\mu, \sigma^2) = \frac{1}{\sqrt{(2\pi\sigma^2)^X}} \exp\left[-\frac{(\ln X - \mu)^2}{2\sigma^2}\right], \quad (3.1)$$

where the scale parameter  $\mu$  is interpreted as the mean of the random variable's logarithm, the shape parameter  $\sigma$  is interpreted as the standard deviation of the random variable's logarithm, shown in Fig. 3.7. As the parameters change in value, different probability distributions are generated. In this case, parameter estimation, a procedure of finding parameter values of a model that best fits the data, is vital to the following analysis.

In order to find parameters best fit our collected data, maximum likelihood estimation (MLE) stands out from other methods of parameter estimation for its following properties: sufficiency (complete information about the parameter of interest contained in its MLE estimator); consistency (true parameter value that generated the data recovered asymptotically, i.e. for data of sufficiently large samples); efficiency (lowest-possible variance of parameter estimates achieved asymptotically); and parameterization invariance (same MLE solution obtained independent of the parametrization used) [62].

MLE estimators need not exist nor be unique. It can be calculated by solving this inverse problem: given the observed data and a model of interest, find the one PDF, among all the probability densities that the model prescribes, that is most likely to have produced data. To compute the maximum likelihood estimators, we start with the likelihood function. By taking the product of the probability densities of the individual  $X_i$  ( $i = 1, 2, 3, \dots, n$ ), we derived the likelihood function of the lognormal distribution for a series of  $X_i$ s. The likelihood function  $L(\mu, \sigma^2|X)$  is defined by reversing the roles of data vector and parameter vector:

$$L(\mu, \sigma^2|X) = \prod_{i=1}^n [f(X_i|\mu, \sigma^2)]. \quad (3.2)$$

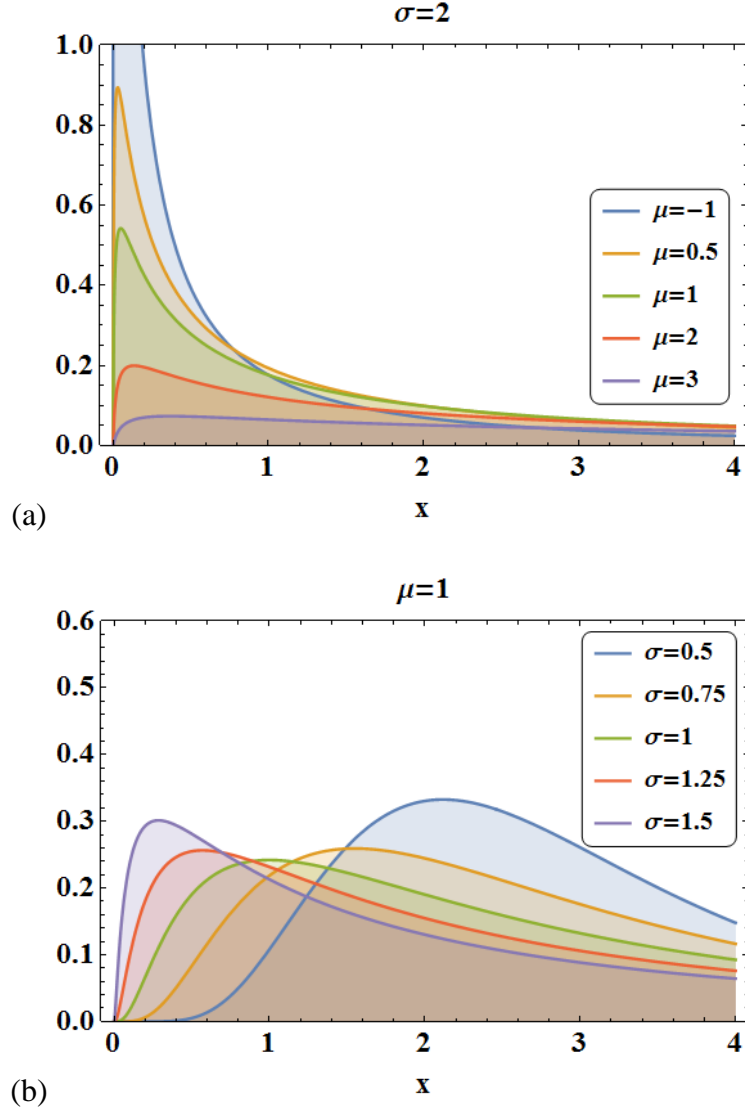


**Fig. 3.7** Some lognormal density plots,  $\sigma = 2$  and  $\mu = 1$  .

By taking the natural log of the likelihood function and taking the gradient of  $L$  with respect to  $\mu$  and  $\sigma^2$  while setting it equal to zero, we can find  $\mu$  and  $\sigma^2$  which maximize  $L$  [63]:

$$\hat{\mu} = \frac{\sum_{i=1}^n \ln(X_i)}{n} \text{ and} \quad (3.3)$$

$$\hat{\sigma}^2 = \frac{\sum_{i=1}^n (\ln(X_i) - \frac{\sum_{i=1}^n \ln(X_i)}{n})^2}{n}. \quad (3.4)$$

To measure the linear relationship between variables, the Pearson's correlation coefficient  $r$  is used in our research. The correlation coefficient is a rescaled covariance:

$$r_{X,Y} = \frac{\text{cov}(X,Y)}{\sigma_X \sigma_Y}, \quad (3.5)$$

where  $\text{cov}(X, Y)$  is the sample covariance, and  $\sigma_X$  and  $\sigma_Y$  are sample standard deviations. After rescaling the covariance, it ranges between -1 and +1, where 1 is total positive linear correlation, 0 is no linear correlation, and -1 is total negative linear correlation[64], shown in Fig. 3.8. More details can be found in Chapter 5 and Appendix B.

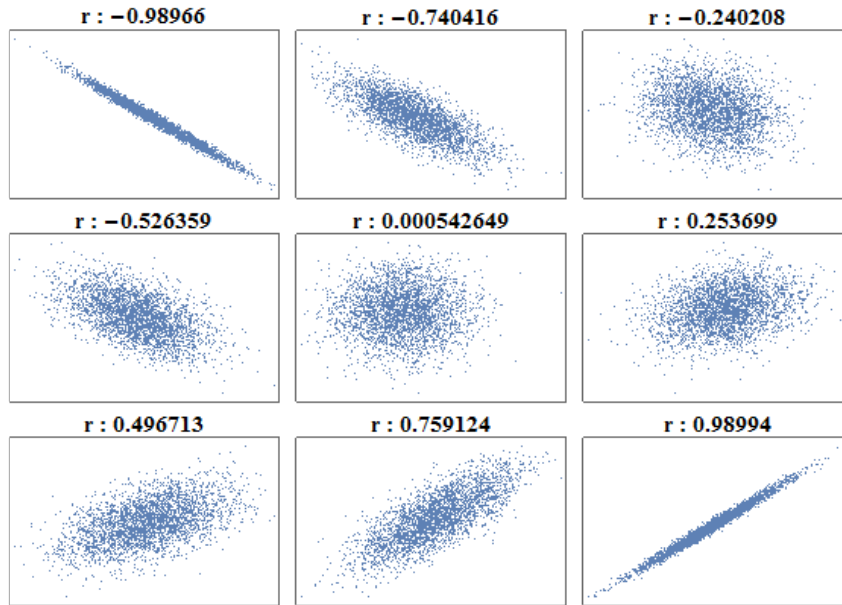


**Fig. 3.8** Correlation coefficient is used to measure linear association.

### 3.3 Summary

The experimental setup, image processing methods, and statistical analysis methods are presented in this chapter. The drainage rate was controlled in the range of 1 ml/min to 20 ml/min and the tilt angle ranged from  $0^\circ$  to  $20^\circ$ , leading to  $Bo^*$  ranging from -0.003 to 0.016. For each experiment, once the pictures were captured by a digital camera, we could apply image analysis techniques to every images and extract relevant data. All methods of data analysis were performed in Mathematica, developed by Wolfram Research of Champaign, Illinois, and all corresponding scripts can be found in Appendixes A-D.

# Chapter 4

## Material Characterisation

In this chapter, material parameters of highly interest in the following statistical analysis are quantified, including the physical properties of both liquid and solid grains. We start by measuring three properties of the liquid used in our study. Then the glass bead properties are quantified with optical methods. Finally, the pore network is generated by employing the image processing methods onto the initially fully saturated frames and a detailed analysis is given in the end.

### 4.1 Liquid

#### 4.1.1 Surface tension

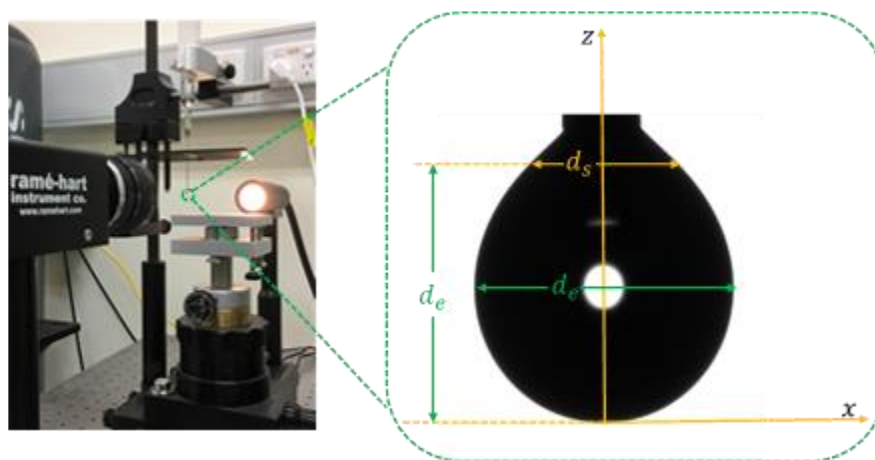


**Fig. 4.1** A pendant drop experiment

Based on the description in Section 2.1.1, after we have known the basic conception of surface tension, we will illustrate the methods to measure surface tension here. Many methods have been proposed for the measurement of surface and interfacial tensions, and each may be said to have advantages for particular applications. Firstly, many solutions were characterised by relatively high viscosity, and by containing material of high molecular weight and thus of low speed of diffusion, including by measuring either the capillary rise or else the hydrostatic

pressure needed to restore the meniscus to its normal level. These methods are not accurate enough because they all depend on an extension of the surface, under such conditions not only would the slow diffusion prevent the attainment of equilibrium, but also the high viscosity would make invalid calibration with free-flowing liquids [65]. A modified method based on measurements of the size and shape of pendant drops was developed by Andreas later [66]. It is more accurate because the surface remains unchanged during the measurement.

Pendant drop method is based on optical analysis the geometry of a pendent drop (shown in Fig. 4.1), even at elevated temperatures and pressures. It is performed by a goniometer (Ramehart, model 200 Standard Contact Angle Goniometer with DROPImage Standard), which can determine the surface tension by measuring the geometry of a pendent drop and knowing the density difference between two liquids. The correlated geometric information of a pendant drop is then explained in the following analysis.

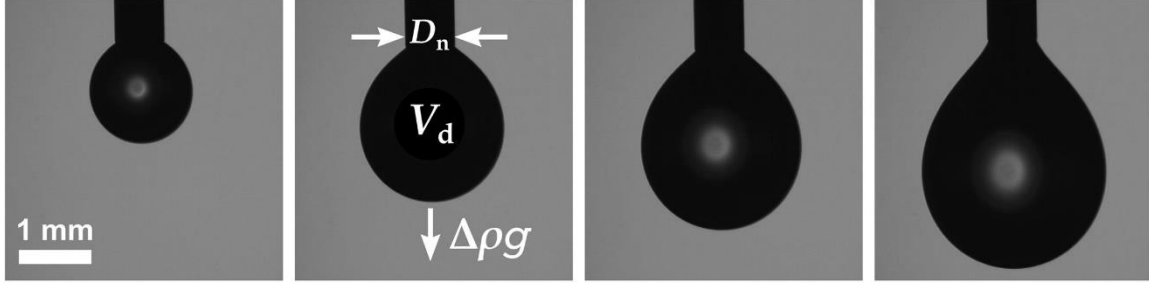
Surface tension is determined in a two-step process. First, the size parameters  $R_0$  and  $\beta$  are determined from the drop profile, after which surface tension is calculated from these parameters by the well-known equation [65]:

$$\gamma = \frac{\Delta\rho g d_e^2}{\beta}, \quad (4.1)$$

where  $\Delta\rho$  is the mass density difference between the drop and the surrounding medium,  $g$  is the gravitational acceleration,  $R_0$  is the radius of curvature at the drop apex, and  $\beta$  is the shape factor, which is calculated from the ratio between the maximum diameter  $d_e$  and the diameter at the distance of the maximum diameter  $d_s$  from the drop apex  $\sigma = d_s/d_e$  (show in Fig. 4.1). The maximum diameter  $d_e$  was found by first finding the (40) points closest to the point of inflection of the curve by the secant method, and then fitting a second-order polynomial through these points, thereby enabling an analytical derivation. A similar technique was used to find the diameter  $d_s$  at the distance  $d_e$  from the apex. From the values of  $d_e$  and  $d_s$ ,  $\beta$  and  $R_0$  were found from Eq. (4.2) and Eq. (4.3), and  $\gamma$  was determined from Eq. (4.1) as

$$\beta = 0.12836 - 0.7577\sigma + 1.7713\sigma^2 - 0.5426\sigma^3 \quad (4.2)$$

$$d_e/2R_0 = 0.9987 + 0.1971\beta - 0.0734\beta^2 + 0.34708\beta^3. \quad (4.3)$$



In our study, we applied 50 separate tests and take the mean value for our dyed liquid surface tension, which is 64.27 mN/m. To characterise the precision, we introduce a non-dimensional parameter, the Worthington number  $Wo$ , to account for the volume effect [67]:

$$Wo = \frac{\Delta\rho g V_d}{\pi\gamma D_n} \quad (4.4)$$

where  $D_n$  is the diameter of the needle and  $V_d$  is the volume of pendant drop. The number  $Wo$  scales from 0 to 1, where large values of  $Wo$  indicate the greatest precision. In our experiment, the needle diameter  $D_n$  is 1mm and the pendant drop volume can be read from micro syringe (Rame-hart, micro syringe 100-10-20) with manual dispensing. The volumes dispensed from the needle are accurate within 0.5%. For every individual measurement,  $Wo$  is larger than 0.5, which is relatively accurate.

#### 4.1.2 Contact angle

The simplest way of measuring the contact angle of a sessile drop is also with a goniometer (see Fig. 4.2), which allows us to measure the contact angle visually. A droplet is deposited by a syringe which is positioned above the sample surface, and a high resolution camera captures the image of the profile from front or side views. The angle formed between the liquid-solid interface and the liquid-vapour interface is the contact angle, which is determined by Young-Laplace equation[68]. The image can then be analysed by using DROPimage (an image analysis software built in the model) [69]. The test liquid and solid substrate used in our experiments are dyed liquid and glass plates, respectively. Since the solid materials of walls and grains in the Hele-Shaw cell are also glass, we only use one kind of substrates to measure contact angle.

The theoretical description of contact angle arises from the consideration of thermodynamic equilibrium among the gas phase (G), the liquid phase (L) and the solid phase(S). In Fig. 4.2, the solid-gas interfacial energy is denoted by  $\gamma_{SG}$ , the solid-liquid interfacial energy by  $\gamma_{SL}$  and

the liquid-gas interfacial energy by  $\gamma_{LG}$ . The equilibrium contact angle  $\theta_C$  is determined by the following equation:

$$\gamma_{SG} - \gamma_{SL} - \gamma_{LG} \cos \theta_C = 0. \quad (4.5)$$

The solid lines in Fig. 4.2 are fitted curve and lines by DROPimage. In order to improve accuracy, we applied 10 measurements of each group of experiments and took 5 separate groups. Finally, we took the mean value from these 50 values, which is  $44.56^\circ$  (std=0.18).



**Fig. 4.2** Image of a dyed liquid drop on the glass plate

### 4.1.3 Viscosity

In order to measure the viscosity of our dyed liquid, we use a concentric cylinder rheometer (Anton Paar MCR502). As shown in Fig. 4.3(b), the liquid is placed within the annulus of one cylinder inside another. The inner cylinder is rotated at a set speed, which determines the shear rate inside the annulus. The liquid in the annulus tends to drag the outer cylinder round, and the torque exerted on the outer cylinder is measured, which can be converted to shear stress.

Due to the low proportion of dye in our liquid, the viscosity of the dyed liquid is close to the viscosity of water at same temperature (see Fig. 4.4). And the dyed liquid is still Newtonian fluid. In other words, the viscosity of liquid doesn't change significantly under different shear rates. The orange dots are experimental data with dyed liquid viscosity under different shear rates, while the red line is estimated viscosity from rheometer ( $\mu = 0.95$  mPa.s).

In Fig. 4.4, the orange dots (experimental data) are almost a plateau within a specific viscosity range: 0.9 to 1.0. As the shear rate increases, rod climbing phenomenon can be found during the measurement. This causes experimental error to our results, also known as end effects in a concentric cylinder apparatus. At high shear rates, elastic materials will climb up a rotating inner cylinder or even leave the apparatus, leading to the deviation of the experimental data from the analytical value (shown in Fig. 4.4) [70].

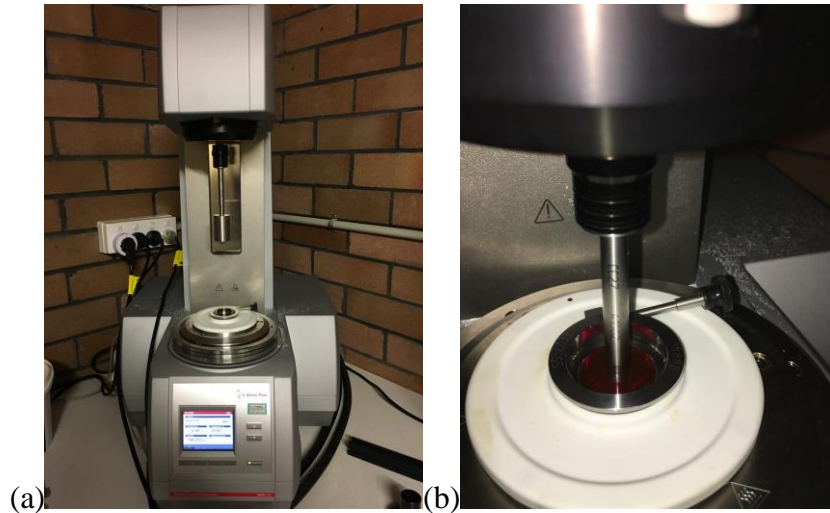


**Fig 4.3** (a) Concentric cylinder rheometer (b) Picture of the dyed liquid in the cup

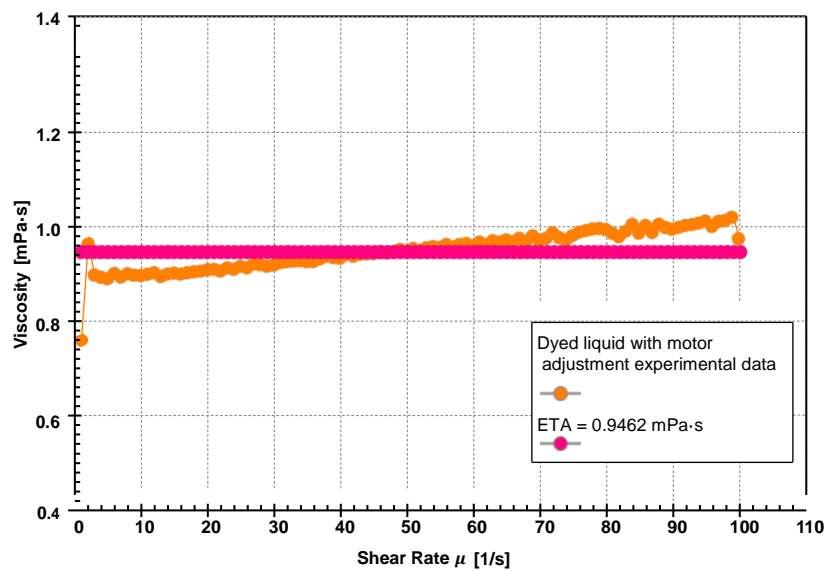


**Fig. 4.4** The viscosity curve of dyed liquid

## 4.2 Morphological analysis of glass beads

To analysis the morphological characteristics, we use a high sensitivity, high resolution analytical instrument for differentiating and characterising particulate samples: Morphologi G3 (Malvern Instruments Ltd, UK). Morphologi G3 gives us data which are generated on individual particles as well as on the samples as a whole. To make our sample has enough individual glass beads and to help the instrument separate different particles easily, we prepared the sample by placing 68 glass beads on a smooth glass plate and checking the dispersion of the sample carefully. By choosing bottom light as the light source and a correct magnification (2.5X), the most appropriate threshold to differentiate solid grains and background could be found by taking a picture from a single glass bead (shown as inset pictures in Fig. 4.5(b)). After scanning the related region and deleting the particles with extremely small areas compared with glass beads (noise of dirt), the distributions of particle area and circularity are shown in Fig. 4.5. The area mentioned here is the visual projected area of the particle.

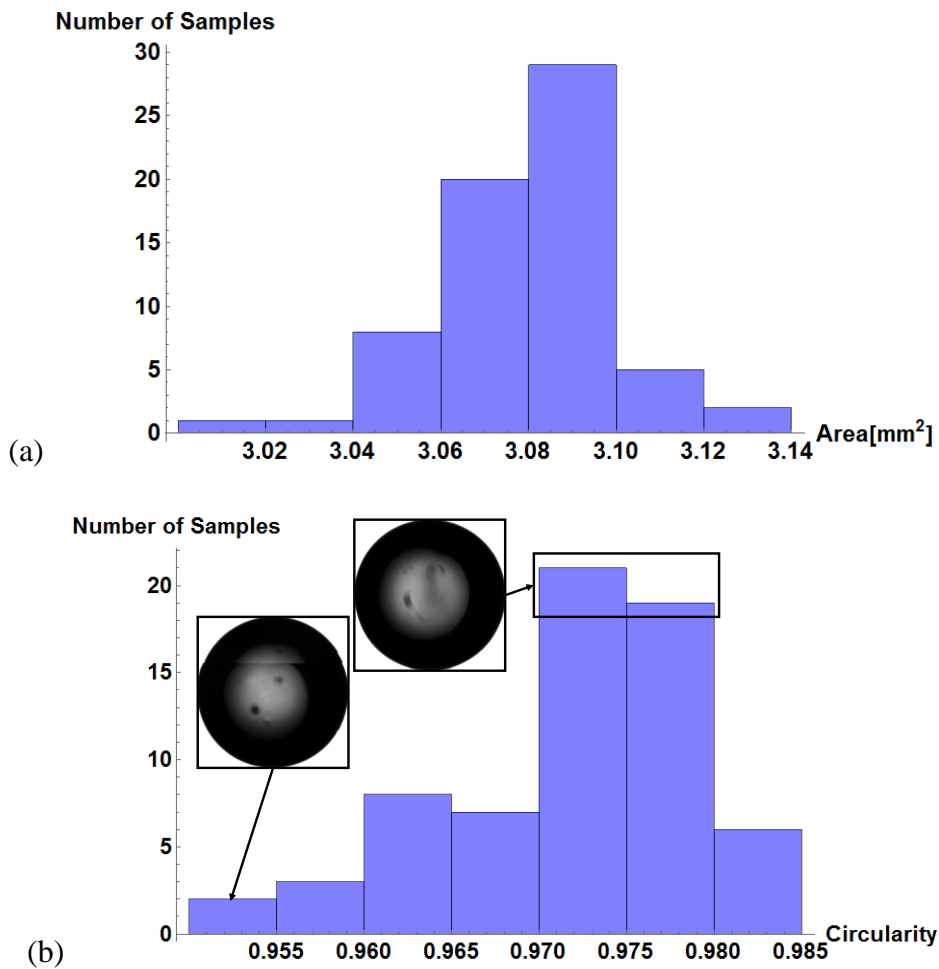
In Fig. 4.5(a), more than a half particles distributed between 3.06 mm<sup>2</sup> to 3.10 mm<sup>2</sup>. The mean and standard deviation values for this dataset are 3.08 mm<sup>2</sup> and 0.02 mm<sup>2</sup>, respectively. The low value of standard deviation indicates that the data points tend to be close to the mean value, i.e., the cross sectional areas of the glass beads mostly have the values close to 3.08 mm<sup>2</sup>.

Fig. 4.5(b) shows glass bead circularity distribution. Circularity is defined as the ratio of the circumference of a circle equal to the object's projected area to the perimeter of the object. It is calculated as:

$$\text{Circularity} = \frac{2 \times \sqrt{\pi \times \text{Area}}}{\text{Perimeter}}. \quad (4.6)$$

In the inset subfigures in Fig. 4.5, two representative images of glass beads are also displayed. Due to the diameter of the glass bead is larger than the cross boundaries of a single snapshot, we activated the particle stitching function built in Morphologi G3. It separately records all items that cross boundaries and then uses shape recognition algorithms to match them together into single particles. However, the limitations in pattern recognition technology sometimes lead to the distortion of a particle (shown as the inset picture in Fig. 4.5), i.e., the circularity of a glass bead deviates from 1.0. Despite the inaccurate value in this dataset, the standard deviation of it is still very low, which is 0.01. And the mean value is 0.97. Our porous matrix employed

is randomly composed by the aforementioned glass beads. Table. 4.1 shows the material characterisation results of both liquid and glass beads used in our experiment.



**Fig. 4.5** (a) The distribution of glass bead cross section area. (b) The distribution of glass bead circularity.

**Table 4.1** Material characterisation results

Liquid		
Surface Tension (mN/m)	64.27	
Contact Angle(°)	44.56	
Viscosity(mPa·s)	0.95	
Glass Beads		
	Mean	Standard Deviation
Area(mm <sup>2</sup> )	3.08	0.02
Circularity(-)	0.97	0.01

## 4.3 Pore network analysis

### 4.3.1 Voronoi cell distribution

Fig. 4.6(a) shows the probability distribution of Voronoi cell area. The data was acquired from 5 fully saturated pictures, and after merging each dataset together we applied histogram function on the entire dataset. By specifying the bin width at 0.4 mm<sup>2</sup>, the data can be sorted into different sub lists. The probability of each sub list is defined as its frequency in a whole dataset. For the sub lists having mid value close to 5 mm<sup>2</sup>, i.e., the relatively small Voronoi cell, correspond to the crystallised regions in our experimental region. As the Voronoi cell area increases, the void area in an individual cell increases. These associate to the relatively loose packing regions.

The inset small squared pictures in Fig. 4.6(a) are zoomed-in cropped images from a Voronoi tessellation, as shown in Fig. 4.6(b). Different colours are used for different values of void ratio ( $e$ ) of Voronoi cell corresponding to the Voronoi mesh. In Fig. 4.6,  $e_{\max}$  has the value 7.169 and the  $e_{\min}$  has the value 0.103. In the upper square picture, all cells are coloured with dark blue showing that all cells have same void ratio in this region. While for the lower square picture in Fig. 4.6(a), the light blue cell has the largest area compared with dark blue ones. The Voronoi tessellation in Fig. 4.6(b) illustrates the crystalized and non-crystallised region of our whole experimental cell. The region with same colour indicates that the localized cells have same void ratio; while the region colorized with different colours shows that the localized cells have different void ratio values. This packing effect has vital influence

on the saturated cluster distribution. More details can be seen in Chapter 6

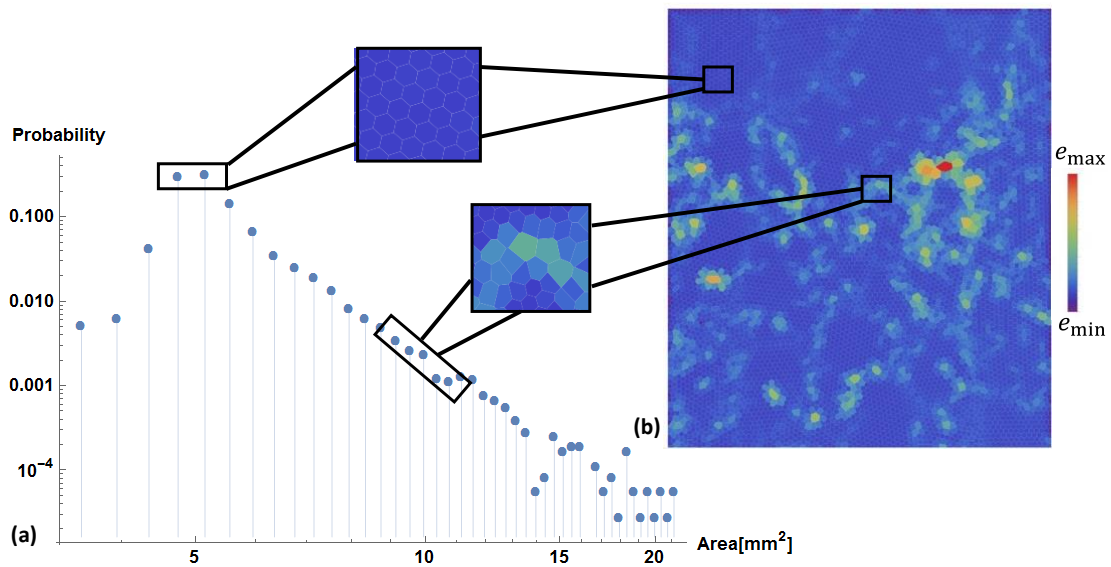


**Fig. 4.6** (a) Voronoi cell area distribution. (b) Map of Voronoi mesh for an individual fully saturated image. The bar legend is scaled in different gradient, ranging from smallest ( $e_{\min} = 0.103$ ) to largest ( $e_{\max} = 7.169$ ) Voronoi cell area.

### 4.3.2 Delaunay triangle distribution

Fig. 4.7(a) shows the probability distribution of Delaunay triangle area. With the same image processing methods mentioned in Chapter 3, the centroids of glass beads are extracted from different saturation level pictures, which are the vertexes of each triangle. The statistical analysis methods used in Fig. 4.6(a) are the same as in Fig. 4.7(a). The largest void ratio for the Delaunay mesh is 11.162; while the smallest void ratio is 0.103, which is hexagonal packing

In Fig. 4.7(b), a pore can be formally seen as the void region inside each Delaunay triangle. Due to the radius of the glass bead is 1mm and the morphological properties for triangle, the void area equals to triangle area minus  $\pi/2$  mm<sup>2</sup>. As a result, the Delaunay triangle area distribution curve in Fig. 4.6(a) can be transformed into pore size distribution curve by adding a negative value ( $\pi/2$ ) on every element in Fig. 4.7(a). The pore size has significant influence on saturated cluster formation and evolution, more details can be seen in Chapter 6.

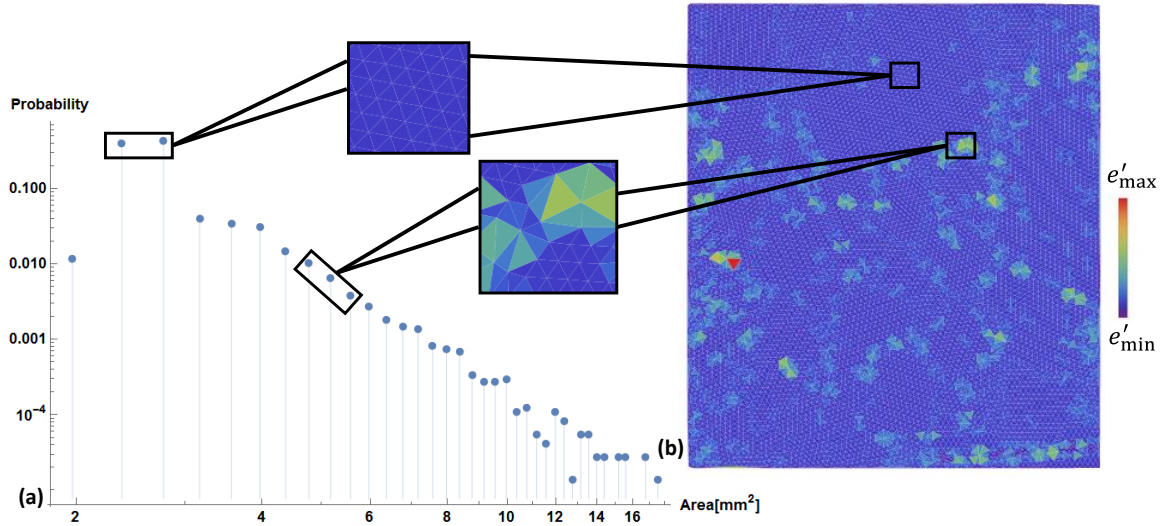


**Fig. 4.7** (a) Delaunay triangulation cell area distribution. (b) Map of Delaunay mesh for an individual fully saturated image. The bar legend is scaled in different gradient, ranging from smallest ( $e'_{\min} = 0.103$ ) to largest ( $e'_{\max} = 11.162$ ) cell void ratio.

## 4.4 Summary

The material characterisation results of both liquid and solid beads used in this study have been presented. Results from Section 4.1 have shown that our dyed liquid has similar properties with water, which indicates that our results could be employed into the water-solid bead systems in future perspectives. Finally, results from pore-network analysis shows that local crystallisation indeed exists in our system which would influence the distribution of saturated clusters in drainage processed. Further results and explanations can be found in Chapter 5 and 6.

# Chapter 5

## Characteristics of Saturated Clusters under Different Drainage Conditions

This chapter quantifies the liquid front morphology characteristics with respect to the applied drainage conditions, presented by  $Bo^*$ , and experimentally evaluates the saturated cluster size distribution and its evolution during drainage processes in wetted granular materials. By comparing the liquid front's morphological characteristics under different  $Bo^*$  values, regulations on the liquid fronts can be returned with respect to  $Bo^*$ . These results provide basis for the following analysis, which is the evolution of saturated cluster distributions in liquid flow cycles as a function of  $Bo^*$ .

### 5.1 Liquid front characteristics with $Bo^*$

As mentioned in Chapter 2, the generalized Bond number has a vital influence on the morphology of liquid fronts during drainage experiments. We use a displacement map as shown in Fig. 5.1 to illustrate this effect. The figure displays experiments for various saturations and generalised numbers. Each picture in Fig. 5.1 is transformed from a RGB image with  $4000 \times 6000$  pixels and rescaled. The light grey regions correspond to the dried regions and the dark grey regions correspond to the locally saturated regions while the different pixel intensities in the grayscale pictures display the frequency of light sources of the experimental setup. The pictures shown here correspond to experiments with the same  $Bo^*$  values in Table. 3.1. The columns of the figure correspond to the saturation level  $S_r$ , which is the volume of water in the experimental cell during the experiment. The rows of the figure correspond to the generalized Bond number  $Bo^* = Bo - Ca$ . The maximum accessible Bond number is related to the maximum inclination angle ( $30^\circ$ ). The negative generalized Bond numbers are all at zero inclination angle, i.e.  $Bo^* = -Ca$ . To minimize the boundary effects, we trim each picture with the dashed green sub-window shown as the picture in the top left corner in Fig. 5.1, which can exclude the inlet/outlet of the experimental cell at the bottom.

At the same level of saturation, the profile of liquid distribution varies with  $Bo^*$ . For negative generalized Bond numbers with large absolute values, more air clusters can be found in the region behind the liquid front, as shown by the light grey area surrounded by dark grey area in Fig. 5.1. For positive valued  $Bo^*$ , less clusters can be found behind the liquid front.

Different from previous research, we firstly filled our experimental cell with the parameters shown in Table 3.1, i.e. for  $Bo^* = -1.556 \times 10^{-4}$ , we set the experimental cell with zero inclination angle and the injection rate to 1 ml/min. Then for the drainage process, we changed the flow direction of the pump after the liquid front reached the top of the experimental cell. The inclination angle and flow rate for both injection and drainage processes are exactly the same. In this case, the distribution of air clusters is determined by the interplay of viscous, gravitational and capillary forces in the experimental cell, which can be quantified by  $Bo^*$ . As the gravitational component increases for a given flow speed (thus, following a column in Fig. 5.1 from bottom to top), the air clusters trapped behind the liquid front is observed to be less in both area and quantity. Besides, the displacement front is observed to evolve from narrow branched fingers to a relatively flat geometry.

To estimate the accuracy of the our image processing methods, Fig. 5.2 shows the liquid saturation calculated from the pump in comparison to the liquid saturation obtained from image-based processing of the entire experimental region for the drainage-injection cycles with different capillary numbers,  $Ca$ . The ratio between the total volume of water and void is quantified by liquid saturation ( $S_r$ ) defined in Eq. (2.6). The image based total volume of void is calculated by multiplying the depth of the experimental cell (2 mm) and the void projection area, which is determined by removing the projection area of all solid beads from the whole projection area of the experimental cell. The pump based total volume of voids is calculated by multiplying the porosity  $n$  and the total experimental cell volume.

The upper branch of each hysteresis curve is the injection section and the lower one is the drainage section. Due to the removal of trapped liquid volume, which usually exists as liquid bridges between grains that can only be observed during drainage processes, the accumulated saturated area of drainage processes is expected to be smaller than the accumulated area of injection processes.

Fig. 5.2(a) is the injection-withdrawal curve for the horizontally placed experimental cell, i.e.  $Bo^* = -Ca$ ; Fig. 5.2(b) is the injection-withdrawal curve for the experimental cell placed with an inclination angle ( $30^\circ$ ), i.e.  $Bo = 0.030$ . The  $Ca$  is determined only by flow rate in

porous medium, thus the four  $Ca$  values shown in Fig. 5.2 are flow rates with 1 ml/min, 2 ml/min, 5 ml/min, 10 ml/min respectively. Each dot is an individual image of the liquid content profile. We applied different time intervals for image capture based on different flow rates. The time intervals for flow rates with 1 ml/min, 2 ml/min, 5 ml/min and 10 ml/min are 20 s, 20 s, 10 s and 2 s respectively. The black dashed line indicates when the points for these two saturation levels are equal.

For Fig. 5.2(a), the impact of  $Ca$  on different drainage-injection curves is driven by the contribution of drainage rates. When  $Ca$  (or the drainage rate) is extremely small, i.e.  $Ca = 1.556 \times 10^{-4}$ , due to the slow flow rate, more water is trapped in the form of liquid bridges at a given saturation, the blue curve shows a noticeable difference compared with other cases. As  $Ca$  is increased, the curves are overlaid with each other and shifted closer to the black dashed line, the liquid saturation of drainage-injection range stays constant at around 0.25-0.85. For Fig. 5.2(b), all the four curves are overlaid with each other and are all located close to the black dashed line. That is to say, for the four series of experiments all water content profiles extracted from images equal to water content profiles computed from flow rates.

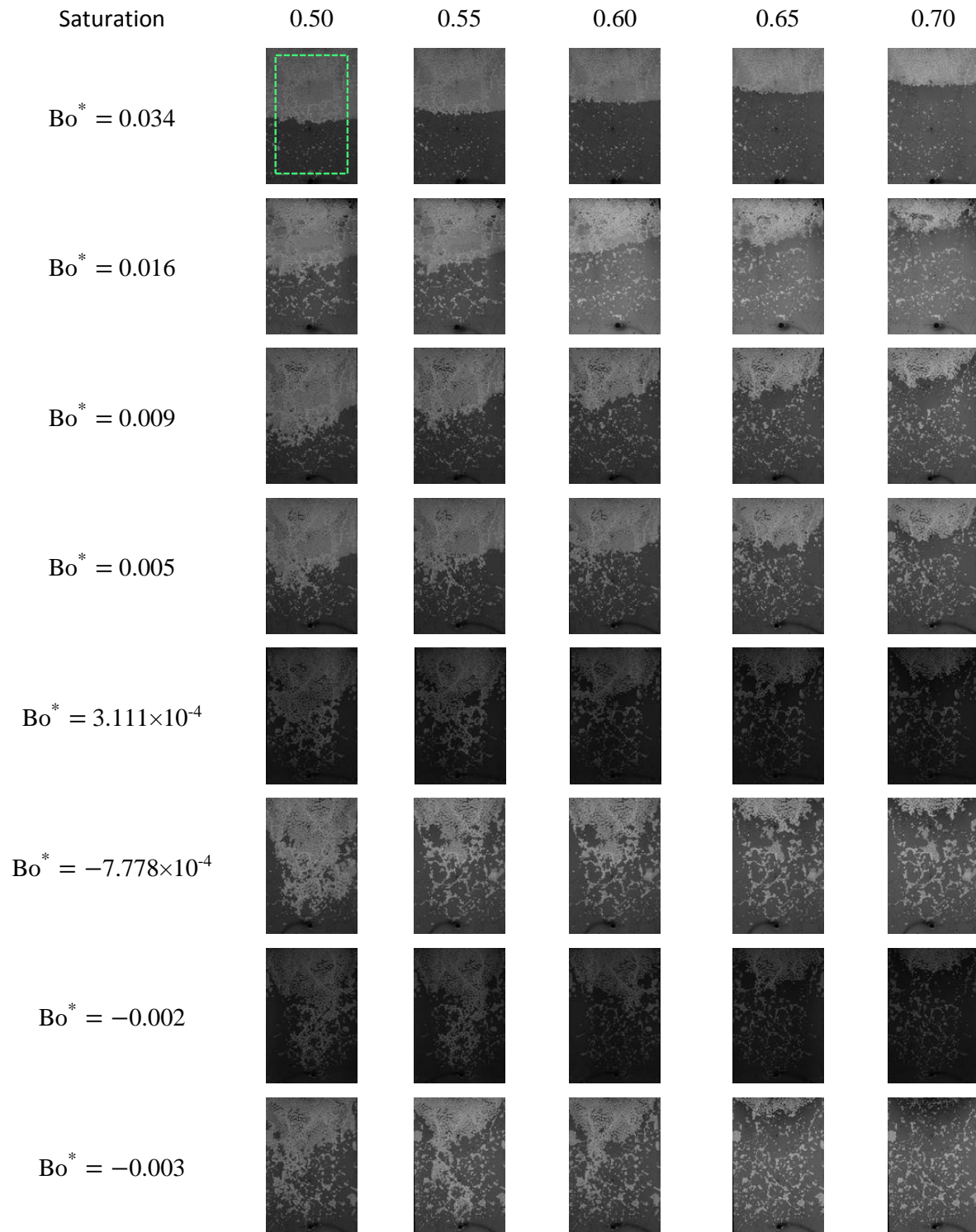


**Fig. 5.1** Displacement structure for 5 series of experiments at saturation  $S_r \cong 0.5, 0.55, 0.6, 0.65$  and  $0.7$ , respectively. Each picture is resized and transformed into grayscales according to the pixel intensity for each channel in the original pictures. The green dashed window in the top left image is the region of interest for all series. The light grey region corresponds to the dried and the dark grey region corresponds to the locally saturated region in each picture.

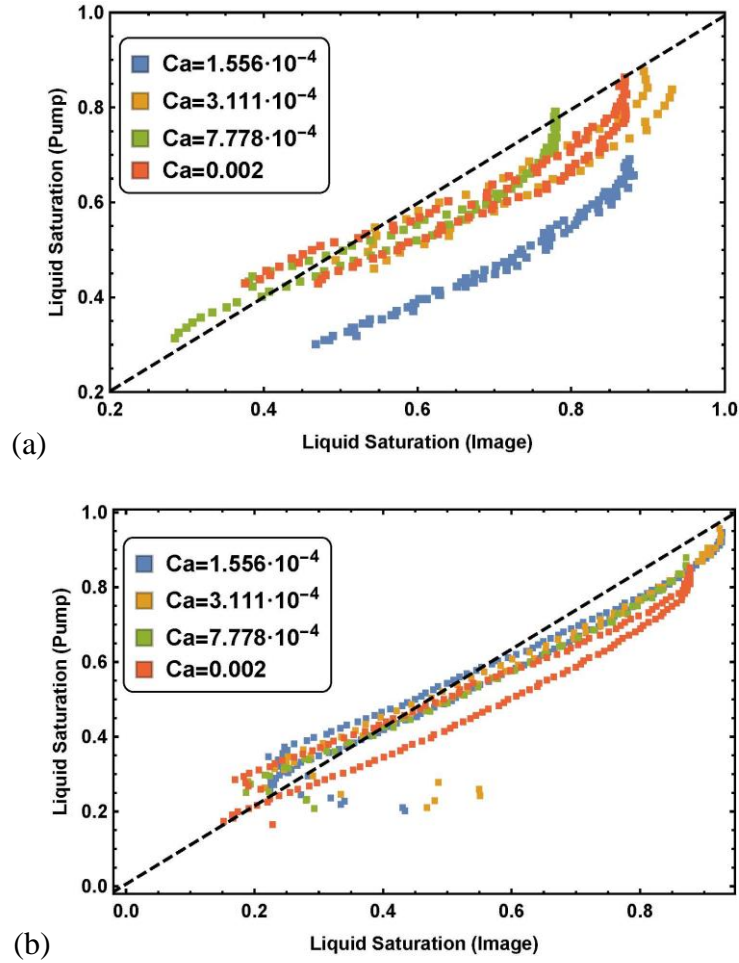


**Fig. 5.2** Liquid saturation obtained from pump and image separately during drainage-injection cycles for different drainage rates (1 ml/min, 2 ml/min, 5 ml/min, 10 ml/min). (a) The experimental cell was horizontally placed, i.e.  $Bo^* = -Ca$ . Each dot is an individual image of the liquid content profile. The black dashed line indicates the points for these two saturation levels equal with each other. (b) The experimental cell was placed with a tilt angle ( $30^\circ$ ), i.e.  $Bo = 0.030$ . The corresponding  $Bo^*$  can be defined with:  $Bo^* = 0.030 - Ca$ . These calibration experiments are not referenced in Table. 3.1.

## 5.2 Saturated cluster size distribution

The saturated clusters are statistically analysed in terms of geometrical properties. The largest saturated cluster in each image, corresponding to the saturated region behind the continuous liquid front, is excluded from the statistical analysis of cluster sizes. Here, we first look at the effective size of the saturated clusters, which is acquired by first collecting the number of pixels

in a localized saturated region and then divided by the spatial resolution 30 pixels per  $\text{mm}^2$ . The unit of all the elements in a single data-set would then be transformed from number of pixel to  $\text{mm}^2$ .

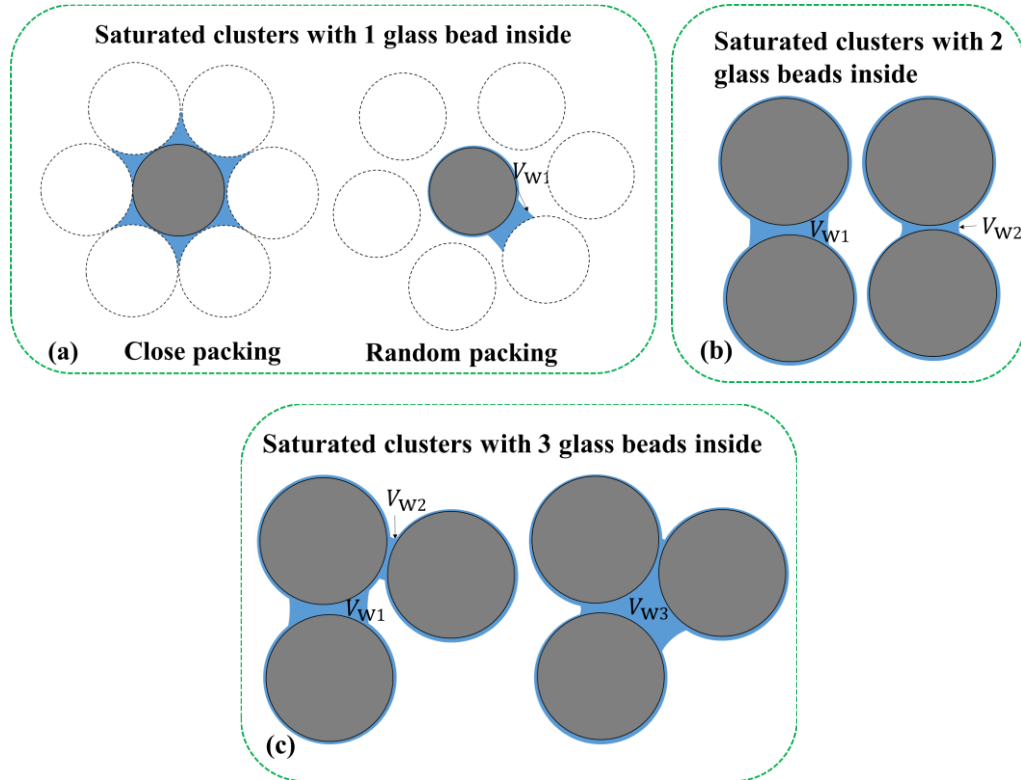


**Fig. 5.3** A few types of observed saturated clusters in the experimental cell.

To get enough data, we did five experiments under the same conditions. By grouping pictures with the same saturation and  $Bo^*$ , we can have the saturated cluster distribution map with both positive and negative  $Bo^*$  values shown in Fig. 5.4 and Fig. 5.5. By rearranging the experimental data into multiple sub-lists by a given bin size, the size distributions of saturated clusters for drainage experiments under different  $Bo^*$  values are depicted.

Fig. 5.3 shows some observed existence of saturated clusters having one to three glass beads inside during drainage processes. In the left subfigure in Fig. 5.3(a), the central glass bead and its neighbouring pore spaces are fully coated and occupied by the dyed liquid. According to the aforementioned imaging processing methods we applied to the pictures, glass beads without liquid coating would be defined as the non-wetting phase. This is due to the fact that the non-coated glass beads have the same pixel intensity as the air phase. In this subfigure, the saturated

cluster is defined as the combination of the central glass bead and all its neighbouring pore spaces. The right subfigure in Fig. 5.3(a) is another configuration of saturated cluster including one glass bead. Fig. 5.3(b) are saturated clusters with two glass beads inside. The distance between two neighbouring glass beads in Fig. 5.3(b) is different. As a result, the volumes of liquid in the pore link between two glass beads in Fig. 5.3(b) are also different, which can be quantified by the projection area of saturated clusters. Fig. 5.3(c) is saturated clusters with three glass beads inside. We assume that the pore structure in these two subfigures are same. However, owing to the fact that the capillary effect in porous medium can be influenced by multiple factors, including different pore sizes or flow rates and the component of gravity along the flow direction, the projection area of these two saturated clusters are different. These factors can be quantified by one dimensionless parameter  $Bo^*$ . In what follows, saturated clusters are extracted from every image at different saturations and  $Bo^*$ . By collecting all the data in each image and drawing their probability density distribution plot, it is easy to find an appropriate distribution fitting model. After fitting all the datasets in different series and gathering distribution parameters, a relation can be found between  $Bo^*$  and distribution parameters.

### 5.2.1 Probability density distribution of saturated clusters

Fig. 5.4 and Fig. 5.5 are plots of the probability density distributions of saturated cluster areas during drainage processes for two liquid saturation levels: 0.5 and 0.6. In these figures, the generalized Bond number ranges from  $-0.003$  to  $0.016$  from subfigure (a) to (f), which can be referred to the experiments in Table. 3.1. The dataset in each subfigure also comes from 5 frames with exactly the same conditions. After grouping the dataset with unit width bins equal to  $2.5 \text{ mm}^2$ , the dataset is separated into sub lists. By computing the probability of each sub list, the probability density distributions of saturated cluster area are plotted.

In Fig. 5.4 and Fig. 5.5, the probability density tends to the peak value (0.15-0.2) around 4-10  $\text{mm}^2$  in both Fig. 5.4 and Fig. 5.5. Due to our porous medium is constructed by glass beads with 2 mm in diameter, the highest frequency saturated clusters in the experimental cell can be interpreted as containing 1-3 glass beads inside.

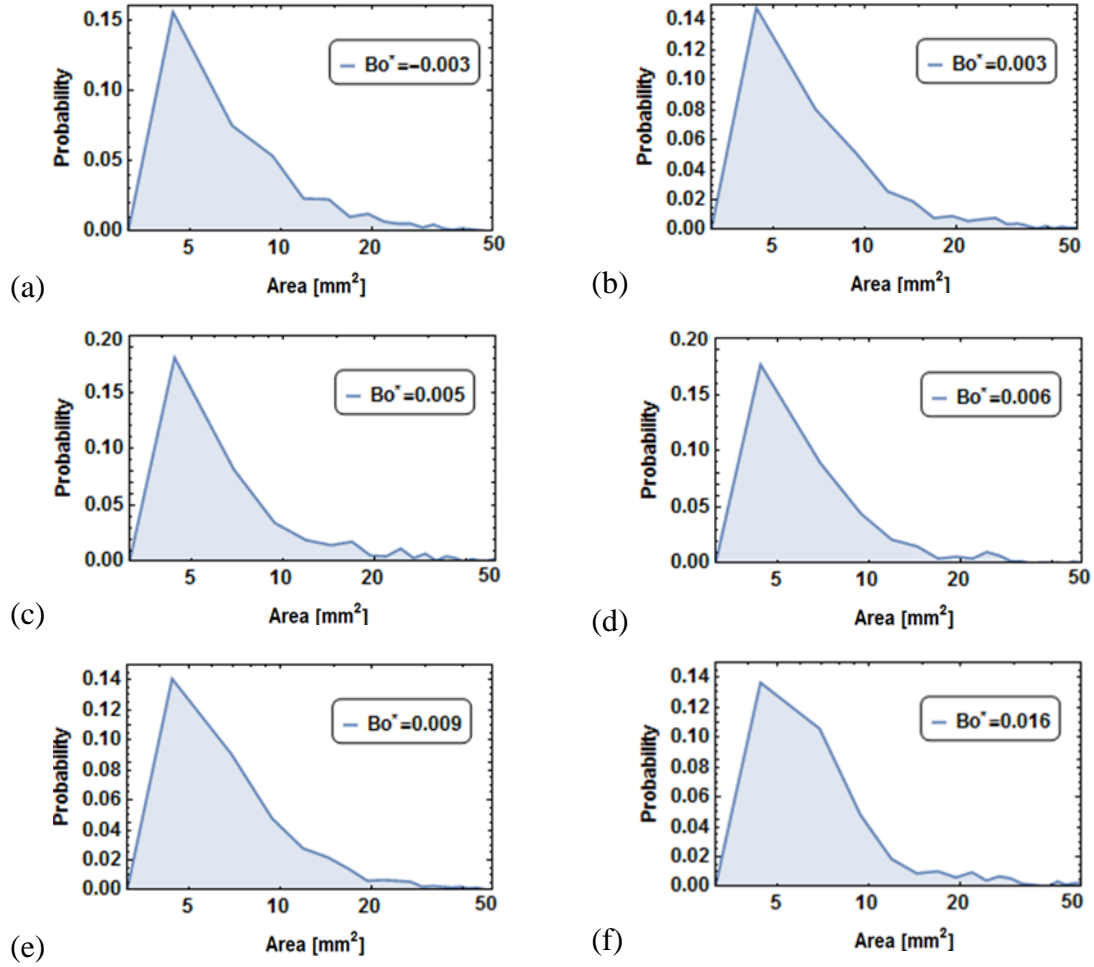


**Fig. 5.4** The probability density distribution of saturated cluster areas during drainage process for liquid saturation level equals 0.5 with different  $Bo^*$  values: (a)  $Bo^* = -0.003$ , (b)  $Bo^* = 0.003$ , (c)  $Bo^* = 0.005$  and (d)  $Bo^* = 0.006$ , (e)  $Bo^* = 0.009$ , (f)  $Bo^* = 0.016$ . The experiments for the different  $Bo^*$  values refer to Table. 3.1.

Besides, we notice that the probability densities of saturated cluster area between 7-10  $mm^2$  in Fig. 5.5 are much larger than the values in Fig. 5.4. This arises from the fact that the liquid redistribution in an existing saturated cluster: at relatively high saturation levels, there are a few big saturated clusters trapped behind the liquid front; however, as the liquid is continuously withdrawing from the bottom of the experimental cell, the variation in the suction stress contributes to the liquid redistribution in the existing saturated clusters. As a result, more

relatively small saturated clusters can be observed at lower saturation levels. This indicates that relatively larger saturated clusters have difficulty in keeping an equilibrium status under different suction stresses.

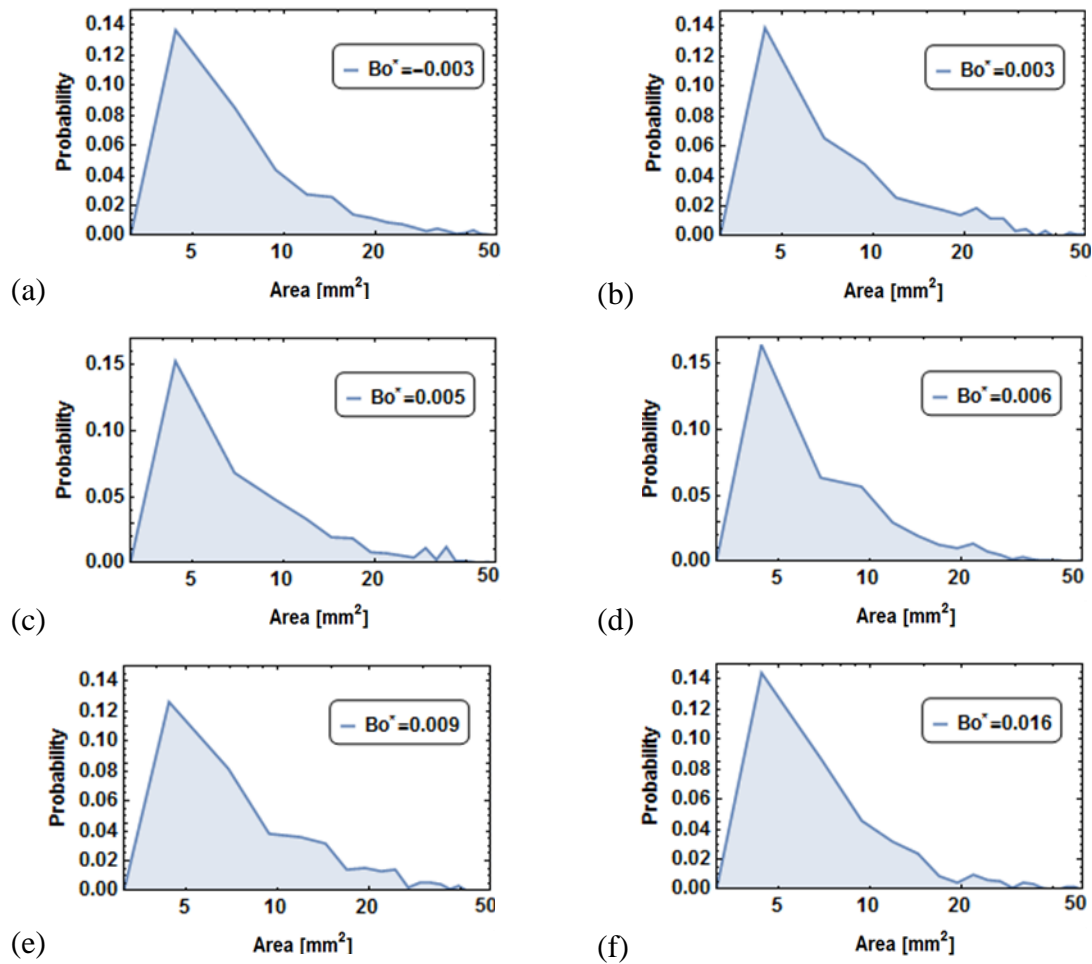


**Fig. 5.5** The probability density distribution of saturated cluster areas during drainage process for liquid saturation level equals 0.6 with different  $Bo^*$  values: (a)  $Bo^* = -0.003$ , (b)  $Bo^* = 0.003$ , (c)  $Bo^* = 0.005$  and (d)  $Bo^* = 0.006$ , (e)  $Bo^* = 0.009$ , (f)  $Bo^* = 0.016$ . The experiments for the different  $Bo^*$  values refer to Table. 3.1.

## 5.2.2 Maximum likelihood fitting

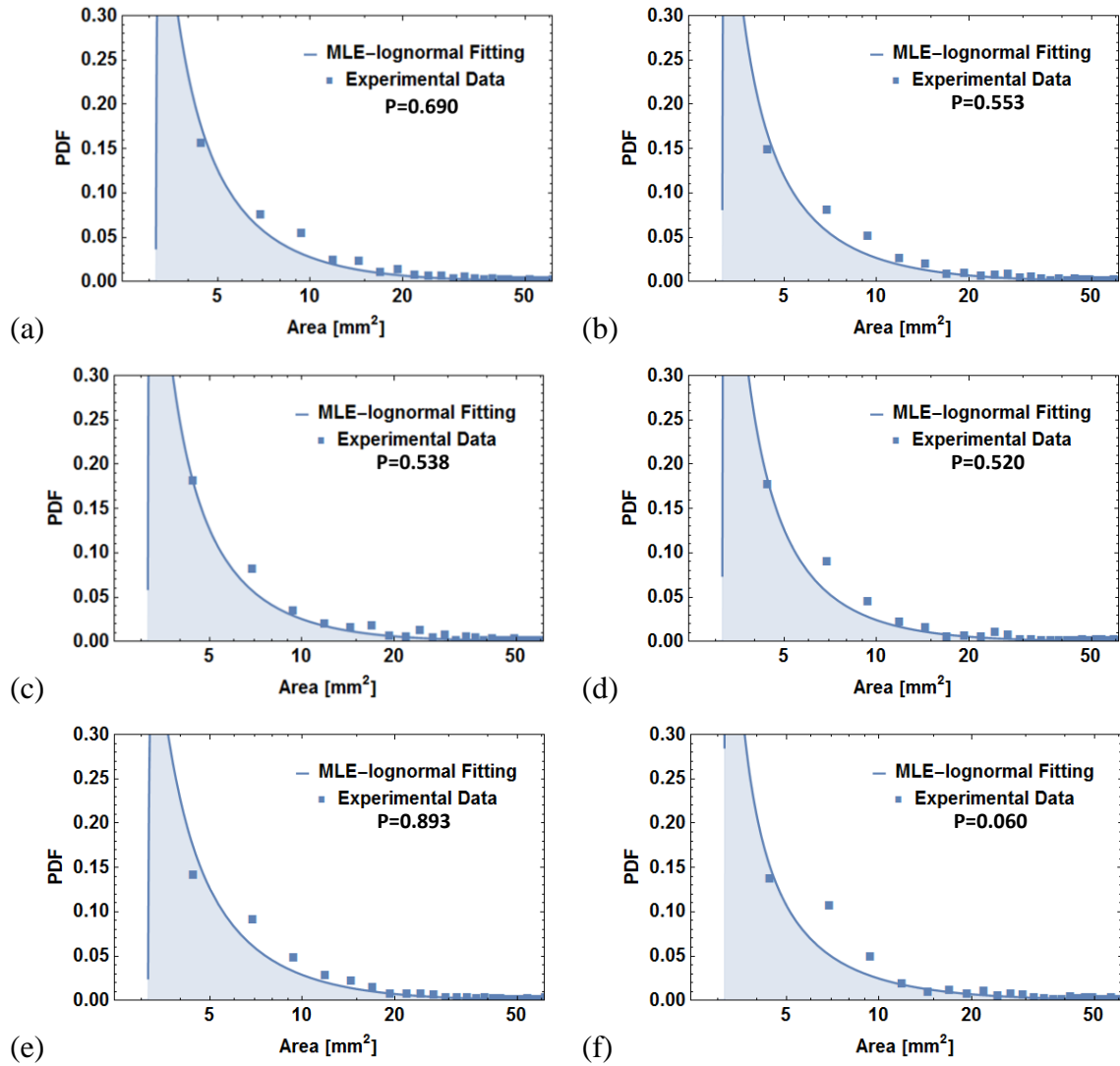


**Fig. 5.6** Log-linear plots of saturated cluster distributions at the same saturation level ( $S_r = 0.50$ ) for drainage processes with (a)  $Bo^* = -0.003$ , (b)  $Bo^* = 0.003$ , (c)  $Bo^* = 0.005$ , (d)  $Bo^* = 0.006$ , (e)  $Bo^* = 0.009$  and (f)  $Bo^* = 0.016$  as a function of area. The dots correspond to the experimental data and the continuous line is obtained by finding the parameter values using maximum likelihood estimation method based on Eq. (3.1).

In Fig. 5.4 and Fig. 5.5, we also notice that the decrease of probability is generated by the sizes of clusters in the log-linear scale. A lognormal distribution function was selected here to best represent the experimental data. In Table. 5.1, goodness-of-fit for three common fitting models are compared and lognormal is selected for its high validity.

As stated in Chapter 3, the lognormal density distribution function has two parameters influencing the geometry of the distribution curve, which are the two variables of the probability density function. To estimate these two parameters of our dataset distribution model from the given observations, as stated in Chapter 3, in statistics we use maximum likelihood estimation (MLE) method, which works by picking the values of the distribution's parameters that make the data "more likely" than any other values of the parameters would make them.

By employing every individual element in a dataset into the lognormal density function and derived the likelihood function by taking the product of all the density functions, we are able to find the particular parameters making the observed results the most probable. The lognormal distribution can then be plotted by substituting the specific parameters acquired from the maximum likelihood estimation method, shown in Fig. 5.6 and Fig. 5.7. These two figures illustrates the saturated cluster probability distribution as a function of area with different generalized Bond number and different saturation levels. In each figure, the generalized Bond number increases from -0.003 to 0.016 from subfigure (a) to (f). To enlarge each dataset with the same generalized Bond number and saturation, we merged data from five pictures from different cycles under the same conditions. Due to the removal of saturated regions that are smaller than a projection area of a typical glass bead ( $\pi \text{ mm}^2$  in this study), as mentioned in Chapter 3, the corresponding fitting curve in each subfigure starts at the point:  $(\pi, 0)$ . Every subfigure is shown with the best fitting curve along with the experimental data points. In each figure, from subfigure (a) to (f), the specific shape of lognormal distribution curve fitting the experimental data varies due to the increment of generalized Bond number. In both Fig. 5.6 and Fig. 5.7, the highest probability of saturated cluster area distribution is located from  $5 \text{ mm}^2$  to  $10 \text{ mm}^2$ , this follows the distribution curve trends in Fig. 5.4 and Fig. 5.3. In addition, the largest probabilities for each subfigure have the value from  $0.25 \text{ mm}^{-1}$  to  $0.4 \text{ mm}^{-1}$ . In other words, more than half of the saturated clusters in each series have the area smaller than  $10 \text{ mm}^2$ . The estimated probability density distribution curves give us adequate description of the data while avoiding the lack of fit for the bin length choosing.

As shown in Fig. 5.1, the smaller the liquid saturation level, the higher the number of saturated clusters trapped behind the liquid front, which makes the sample large enough for an adequate fit using the MLE method. For instance, in Fig. 5.6 and Fig. 5.7 most experimental data points are located along or close to the decreasing branch of the lognormal distribution curve. To guarantee our quality of fit, a goodness-of-fit test is applied on every dataset and the resulting p-value is labelled in each subfigure. It is observed that lower saturation levels exhibit relatively large p-values while higher saturation levels are seen to have small p-values. This can be

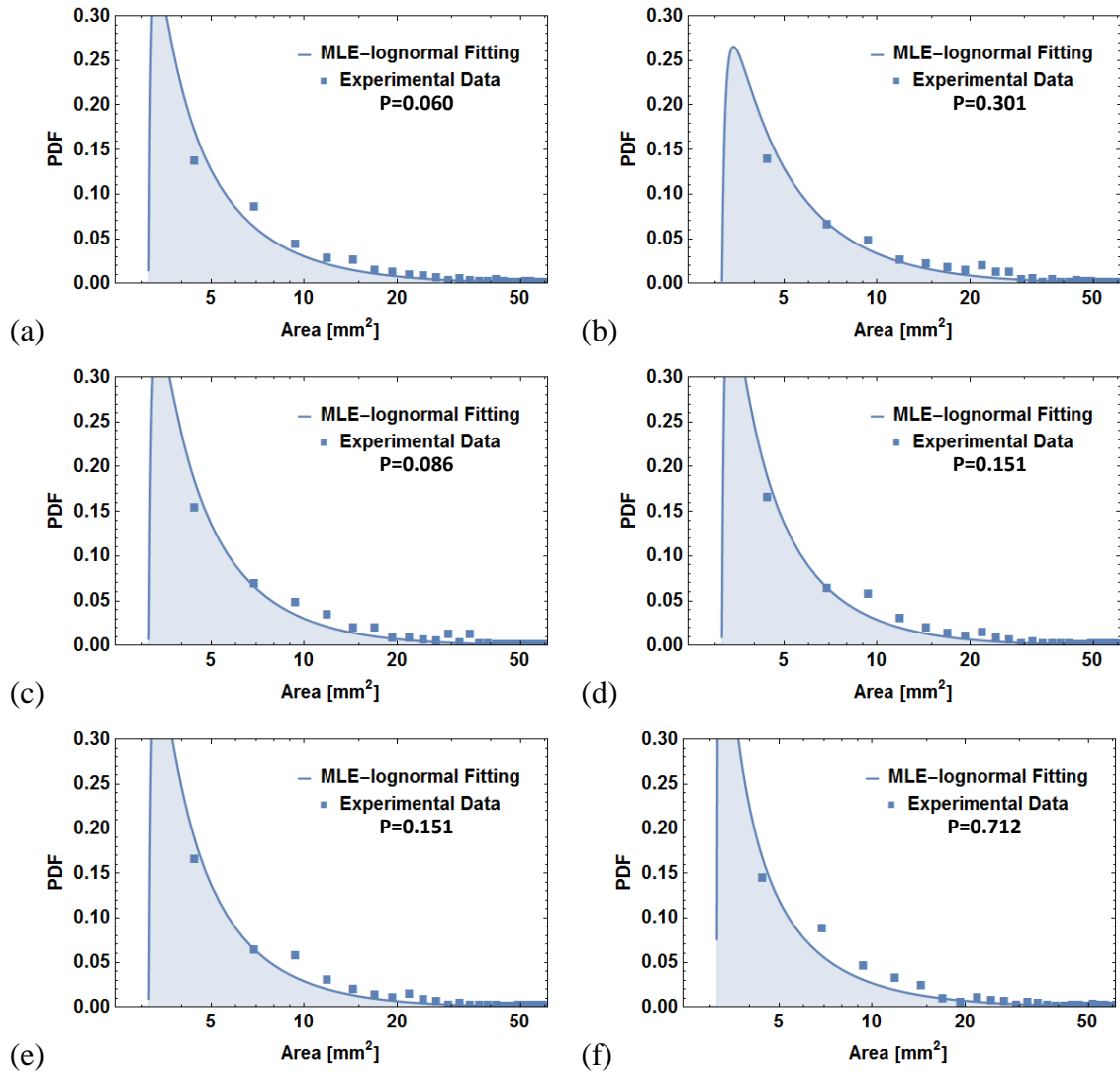


**Fig. 5.7** Log-linear plots of saturated cluster distributions at the same saturation level ( $S_r = 0.60$ ) for drainage process with (a)  $Bo^* = -0.003$ , (b)  $Bo^* = 0.003$ , (c)  $Bo^* = 0.005$ , (d)  $Bo^* = 0.006$ , (e)  $Bo^* = 0.009$  and (f)  $Bo^* = 0.016$  as a function of area. The dots correspond to the experimental data and the continuous line is obtained by applying all experimental data using a maximum likelihood estimation method based on Eq. (3.1).

explained by the fact that more saturated clusters can be observed in lower saturation levels contributing to a more possible assumption of hypothesis. In contrast, there are a few experimental data points deviate from the decreasing branch of the lognormal curve in Fig. 5.7.

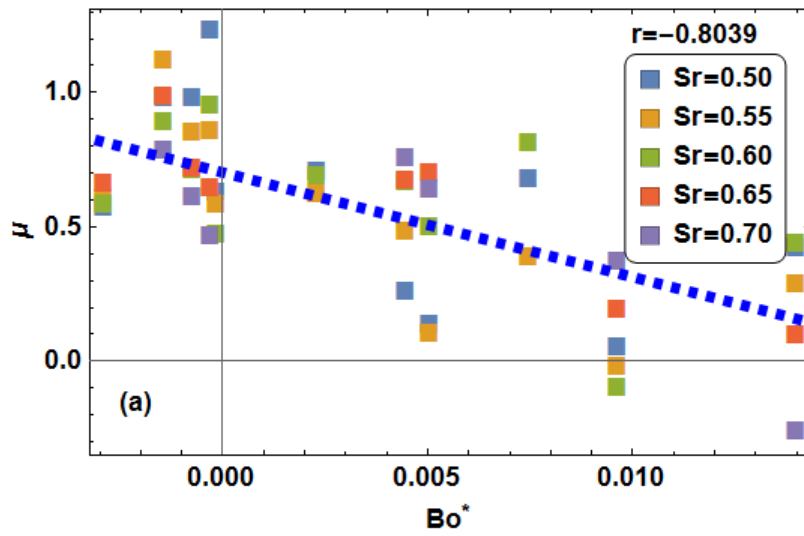
### 5.2.3 Statistical distributions

Table. 5.1 shows two widely used tests, the Pearson's  $\chi^2$  and Anderson-Darling methods to test the validity of three assumed distribution models (Lognormal distribution, Weibull distribution and Gamma distribution). We applied a particular dataset ( $S_r = 0.5$ ;  $Bo^* = -0.003$ ) to the two test methods and listed the resulting values in Table. 5.1. As shown in Table 5.1, the p-values of lognormal distribution for both tests are large enough ( $>0.5$ ) to verify the validity of lognormal distribution, which has been selected on the basis of other prior considerations.

**Table 5.1** Obtained maximum likelihood parameters from a specific data-set. Chi-square test and Anderson-Darling criterion are used to quantify the goodness of fit.

$S_r=0.5$ $Bo^*=-0.003$	Parameter		Pearson's $\chi^2$		Anderson-Darling	
			Statistic	P-value	Statistic	P-value
Lognormal Distribution	$\mu$ = 1.078	$\sigma$ = 1.590	23.841	0.690	0.582	0.665
Weibull Distribution	$\alpha$ = 0.603	$\beta$ = 6.538	97.652	1.213 $\times 10^{-9}$	11.755	3.019 $\times 10^{-4}$
Gamma Distribution	$\alpha$ = 0.463	$\beta$ = 25.444	202.537	2.267 $\times 10^{-9}$	32.2891	0.000

### 5.2.4 Function of $Bo^*$ and $\mu/\sigma$



**Fig. 5.8** Plot of lognormal distribution parameter, scale parameter  $\mu$ , as a function of generalised Bond number,  $Bo^*$ , for different saturation levels, correlation coefficient  $r$  is also provided.

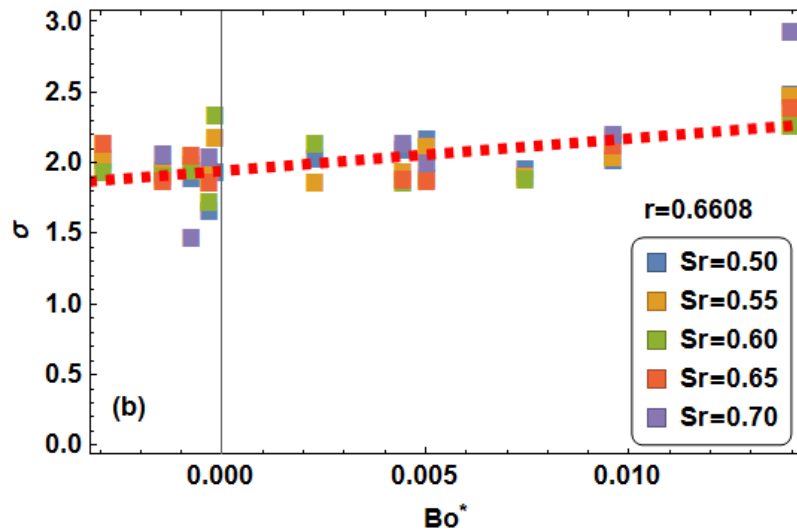


**Fig. 5.9** Plot of lognormal distribution parameter, shape parameter  $\sigma$ , as a function of generalised Bond number,  $Bo^*$ , for different saturation levels, correlation coefficient  $r$  is also provided.

After collecting all the parameters ( $\mu$  and  $\sigma$ , shown in Table. 5.1) for all series in the existing experiments, we introduced the Pearson's correlation coefficient method to quantify their relative linear relationship. As aforementioned in Chapter 3, the Pearson's correlation coefficient quantifies the linear relationship between two variables. To compute the correlation coefficient for both  $\sigma$  and  $\mu$  as a function of  $Bo^*$ , we substitute these two parameter values of all experiments with respect to  $Bo^*$  into Eq. (3.5). The correlated values for both parameters are shown in Fig. 5.8 and Fig. 5.9. In Fig. 5.8, the value of correlation coefficient of  $\mu$  and  $Bo^*$  is  $-0.8039$ , implying that all data points lie close to a line for which  $\mu$  decreases as  $Bo^*$  increases; while in Fig. 5.9, the value of correlation coefficient of  $\sigma$  and  $Bo^*$  is  $0.6608$ , indicating that that all data points also lie close to a line for which  $\sigma$  increases as  $Bo^*$  increases.

In statistics, for a given lognormal distribution,  $\sigma$  and  $\mu$  are, respectively, the mean and standard deviation of the variable's natural logarithm. The linear relationship obtained for the lognormal density function parameters as a function of  $Bo^*$ , is therefore a correlation between the mean and variation of the natural logarithm for saturated clusters sizes. In this case, as  $Bo^*$  increases, the natural logarithm of mean saturated cluster sizes decreases; meanwhile, the natural logarithm of saturated cluster sizes are spread out over a wider range of values.

### 5.3 Discussion

The results showed in this chapter quantitatively depict the effects of complex interplay of multiple mechanisms, i.e., viscous, gravitational and capillary forces, on the formation and evolution of saturated clusters in a porous medium. A linear relationship lies in between the generalized Bond number ( $Bo^*$ ) and saturated cluster size distribution parameters. In other words, by knowing every force in a porous medium we are able to draw the saturation cluster area distribution by computing the correlated parameters. The implication of this predictive distribution for improved characterisation of multiphase flow in porous media is discussed below.

In enhanced oil recovery, the most ideal scenario for the fluid collected from the production well is pure crude oil driven by the water injected from the injection well. However, a complex multiphase system in the oil reservoir made up by air, water, oil and solid grains comes with some capillary effects naturally, for instance, the viscous fingering and oil droplets left behind the continuous interface between water phase and oil phase. These two phenomena would

influence the efficiency in the oil recovery industry. The oil droplets left behind the liquid front not only change the chemical properties by coating the surface of solid grains but also change the pathway of water flow. In this case, it is important to allocate the water injection rate in an appropriate range with knowing conditions. Due to the injection and production wells being on the same plane, the gravitational force can be neglected in the numerical analysis. Different accumulated saturated areas can be computed from the lognormal distribution curves, which are shaped by the parameters. In this way, we are able to minimize the accumulated locally saturated area and improve the efficiency in the industrial operations.

In groundwater flow modelling, saturated clusters are also significant for its existence. In pure groundwater flow modelling, these clusters could be immobile water or stagnant water in a relatively narrow pore space, which could change the pathway for the following water flow. In contaminant transportation modelling, the polluted source is dissolved by the aqueous phase in porous media. Studies have shown that in dissolution experiments, the flowing aqueous phase appeared to infiltrate through the contaminated zones as multiple fingers [7]. Subsequently, trapped contaminated clusters are sure to leave behind the flow interface. To minimize the contaminated area, it is important to find the best flow conditions while making the accumulated trapped cluster area smallest. Our results are able to give a better solution for this problem by computing the most appropriate flow rate for the polluted layer.

In addition, as aforementioned in Chapter 2, the interfacial forces in partially unsaturated soils have significant influence on the resulting effective stresses. Due to the discontinuous liquid phase in the region behind the liquid front, the modified effective stress could be the accumulated value of total stress and suction stress [71]. Besides, corresponding to Likos's results [2], for a given sample and knowing flow conditions, the suction stress in unsaturated soils can be a function of interfacial area. In this case, it is able to refine the traditional effective stress definition in unsaturated soils while considering the interfacial forces. Our results can serve as a bridge to connect the interfacial area for different phases and different flow conditions.

## **5.4 Summary**

In this chapter, we firstly quantified the liquid front morphology characteristics with respect to  $Bo^*$  and experimentally evaluated the saturated cluster size distribution and its evolution during drainage processes of wetted granular materials. The distribution is found to follow a lognormal distribution. It is concluded that the scale parameter  $\mu$  and shape parameter  $\sigma$  negatively and

positively correlate with  $Bo^*$ , respectively. Due to the fact that a strong linear dependence exists between lognormal distribution parameters and generalised Bond number,  $Bo^*$ , it is possible to generate a function containing  $\mu$ ,  $\sigma$  and  $Bo^*$  for describing the cluster distribution at various saturation levels.

# Chapter 6

## Pore-Structure Dependent Saturated Cluster Distribution

The flow of two immiscible fluids through a porous medium depends on not only the complex interplay between viscous, capillary and gravitational forces, but also the packing characteristics of the porous media. The interaction between these forces and the geometry of porous medium contributes to the complex flow regime in porous medium, shown in Fig. 6.1. Four different liquid content regimes, and mentioned in Chapter 2, can be observed in a specific picture. These four regimes can be separated by the projection area due to the different volume of water for the same solid structure.

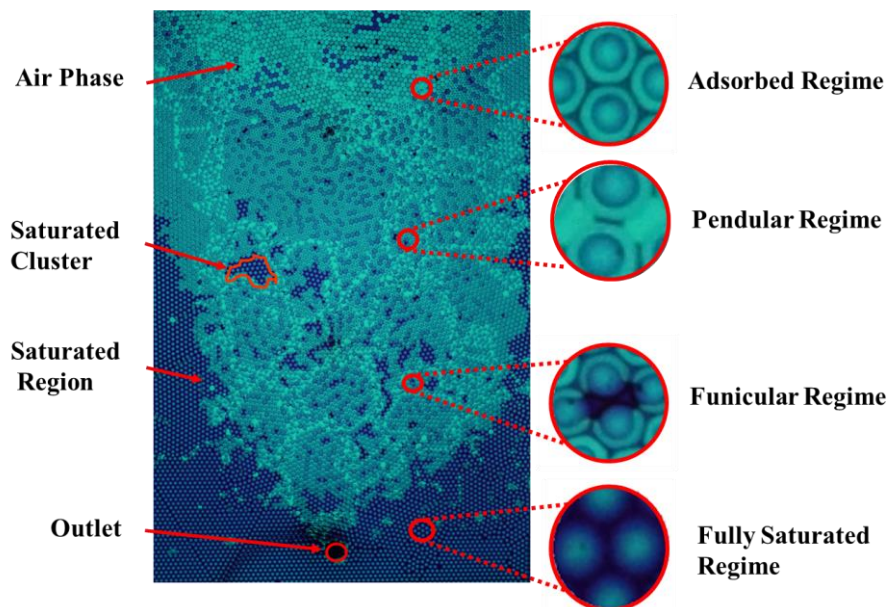


**Fig. 6.1** An example experimental image revealing different saturation regimes

In this chapter, we will focus on the influence of porous medium packing characteristics on the saturated cluster formation and evolution. We used the topological information provided by

Voronoi and Delaunay tessellation to quantify the crystallised and non-crystallised effects on the saturated clusters. The procedures for the data stream calculation and correlated results are also given.

## 6.1 Voronoi and Delaunay tessellation analysis

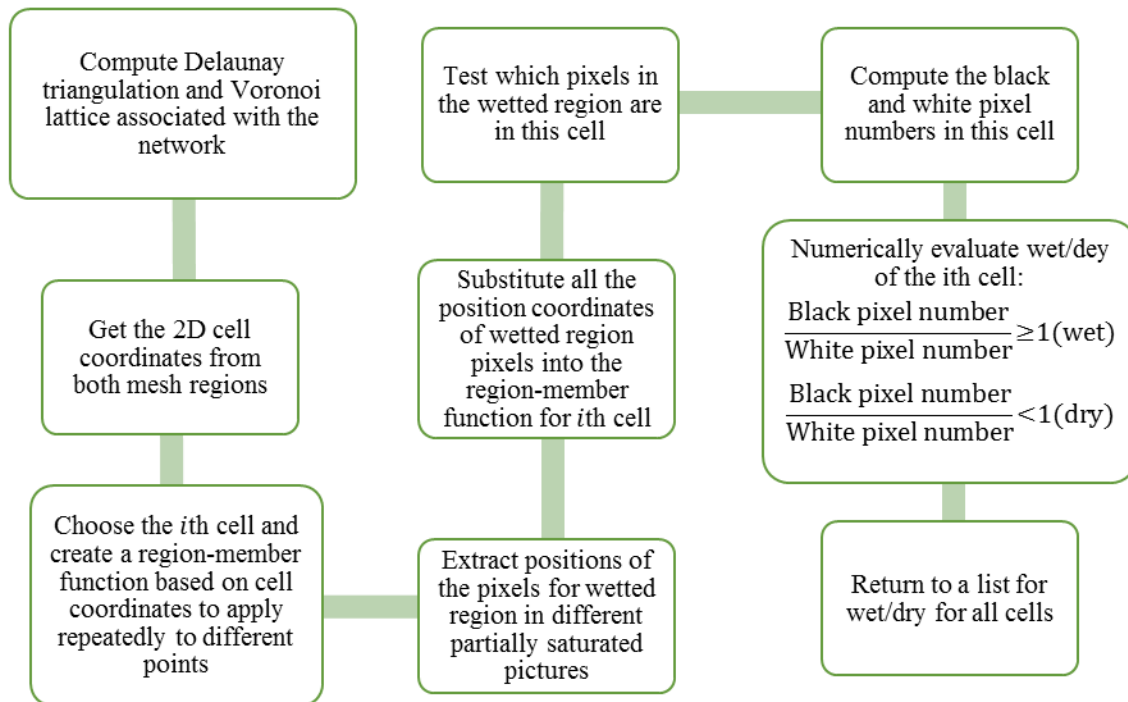


**Fig. 6.2** The flow chart of the pore network analyse method.

The utilisation procedures of using Voronoi and Delaunay tessellation in our statistical analysis are shown in Fig 6.2. We first compute Delaunay triangles and Voronoi cells associated with the network using the image processing method mentioned in Chapter 3. After numbering and collecting the vertex coordinates of every cell in both mesh regions, we are then able to create region-member functions associated to each cell, for instance, the  $i$ -th region-member function for the  $i$ -th cell. The next step is to import all pictures representing different saturation levels and drainage conditions into our calculation. These pictures are then be performed with morphological image processes and transformed into a black and white image, while the black and white pixels stand for dry and wetted regions, respectively. The black islands inside the white area are the wetted clusters trapped in the air during drainage. To allocate our focus on the saturated clusters behind the liquid front, we removed the largest continuous black island

in each black and white picture, leaving other relatively small wetted clusters inside the pictures. With the help of the built-in function (Pixelvaluepositions) in Mathematica, we then extracted all the black pixel positions in every picture. By repeatedly applying different black points into the  $i$ th region-member function, we returned to the results of true or false for whether these points are region members of the  $i$ th cell. This step gave us the results of the amount of points in the  $i$ th cell and we were then able to know the amount of black points in every cell by repeatedly employing this step on all rest cells in an individual picture. As a result, we were able to return to a list of number of black points in each cell aligned with the cell number. By comparing the ratio of black pixel number to white pixel number, we classified the cells into two groups: dry and wet, shown in Fig. 6.2. After filtering the uncorrelated information from the aforementioned steps, we finally came to a list giving the area and wet (1) / dry (0) properties for every cell in an individual picture. To enlarge our dataset, we also did five experiments under same conditions and merged all five lists.

## **6.2 Effect of Voronoi/Delaunay cell area distribution on the wetted cell area distribution**

In Chapter 4, we discussed the packing characters for our experimental samples. In this section, we will look into its influence on saturated cluster formation and evolution during drainage processes. In Fig.6.3 and Fig. 6.4, the continuous pink curves with empty circles in each image are computed from initially fully saturated images with different drainage conditions. The other coloured curves represent wetted cell area distribution within saturated clusters for different saturation levels associated with different drainage conditions. For these cases, the largest continuous saturated region below the liquid front is removed from every picture and only saturated clusters were left behind in each frame. By employing image processing operations on every image, we collected the data stream from five pictures with same flow conditions and merged all sub-lists as the final step. To have a better visualisation of how the data is distributed, we depicted the wetted cell area number distribution curve and wetted cell area probability curve as a function of cell area, shown in Fig. 6.3 and Fig. 6.4.

In Fig. 6.3 and Fig. 6.4, the length interval between two neighbouring points of the continuous lines is  $0.4 \text{ mm}^2$ . In other words, we specified the bin space with  $0.4 \text{ mm}^2$  and collected a list of bins and histogram heights of the values. Due to the removal of the largest saturated region, for smaller saturation levels more accumulated saturated area can be computed from the first

column of figures in Fig. 6.3. This can be explained that the saturated clusters are generated when the constant liquid front met different conductive pathways during drainage processes, which need a long enough distance along the flow direction as a prerequisite condition for the formation of saturated clusters. As to the lower saturation levels, more air phase has been involved into our system. Hence, more resistive pathways are bypassed and subsequently the accumulated area of liquid phase viscous detention also increased.

In addition, for the subfigures in the first column in Fig. 6.3, the  $Bo^*$  is increasing from (a-1) to (e-1). However, the accumulated wetted cell area included in saturated clusters is decreasing. This follows the aforementioned theory about the influence of  $Bo^*$  on geometry of liquid front in Chapter 2: for large negative values of  $Bo^*$ , the capillary fingers are widely spread along the liquid front during drainage processes; for large positive values of  $Bo^*$ , the liquid front is observed as a nearly flat geometry. For flat liquid fronts, gravity is always large enough to stabilise the displacement geometry leading to few saturated clusters trapped behind liquid front and for unstable liquid fronts, more thin fingers can be observed and disconnected from the largest saturated region.

Despite the difference of the accumulated wetted cell area between  $Bo^*$  and saturation levels, the trends and peak values of the probability distribution curves for all cases are located close to each other. Compared Fig. 6.3(a-1) with Fig. 6.3(a-2), it is easy to discover that more than a half cells have area at around 4-6 mm<sup>2</sup>. By removing the projection area of a single glass beads ( $\pi$  mm<sup>2</sup>), the void space in each cell is then between 0.86-2.86 mm<sup>2</sup>. This indicates a relatively close packing correlated to the localised region in the experimental sample. That is to say, the relatively close packing region is more capable to hold liquid than loose packing regions. In addition, it can be observed that for large void ratio cells liquid is trapped only at small generalized Bond number experiments. The volumes of liquid trapped in relatively large void ratio pore cells are consistent with previous theory. As the flow rate increases, the gravitational force is not able to balance the increasing viscous pressure gradient. When the pressure difference exceeds the threshold value, the surrounding pore throats would be invaded by air phase and a viscous finger is then generated. And as the liquid is continually withdrew from the bottom, thin fingers are easily disconnected from the continuous front, leading to more large wetted cells in these drainage conditions.

**Table 6.1** Pore-scale size parameters and wetted probabilities at different individual face area of Voronoi tessellation for  $Bo^* = -0.003$ ,  $S_r=0.5$ .

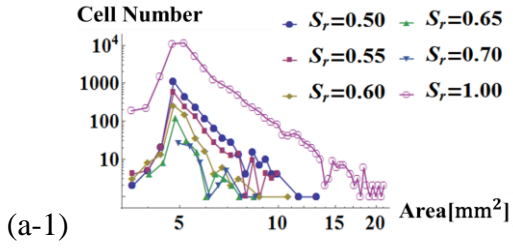
$Bo^* = -0.003$			
Area of Individual Cell (mm <sup>2</sup> )	Wetted Probability (%)	Mean (mm <sup>2</sup> )	Standard Deviation (mm <sup>2</sup> )
$3.14 < A < 4.14$	0.57	3.69	0.30
$4.14 \leq A < 5.14$	3.29	4.78	0.17
$5.14 \leq A < 6.14$	2.32	5.51	0.26
$6.14 \leq A < 7.14$	3.01	6.60	0.28
$7.14 \leq A < 8.14$	1.33	7.57	0.28
$8.14 \leq A < 9.14$	2.41	8.58	0.27
$9.14 \leq A < 10.14$	4.33	9.59	0.25
$10.14 \leq A < 11.14$	0.63	10.64	0.28

Table 6.1 shows the pore-scale size parameters and wetted probabilities for Voronoi cells computed from five pictures. The experiment shown here corresponds to saturation level valued 0.5 and generalized Bond number valued  $-0.003$ .

By grouping all cells with their individual face area, the corresponding dry/wet properties of every cell are also distributed into the same group. As mentioned in Section 6.1, the wet cells are labelled with 1 and dry cells are labelled with 0. By collecting the amount of 1s in an individual group and being divided by the total amount of the cells in a group, the wetted probability for each group is computed.

The relatively large values of wetted probability in Table 6.1 are most widely observed cells in the crystalized region. However, the smaller values are from cells with extremely large or small areas. This trend shows that in our porous medium, the most widely distributed cells have stronger capability of liquid trapping than the extreme regions.

### Wetted Cell Number Distribution



### Probability Distribution

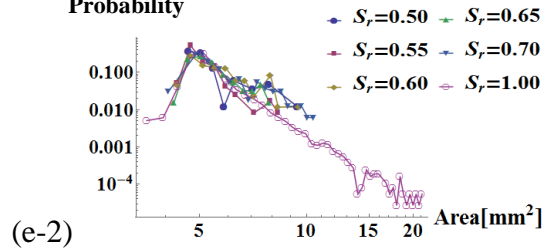
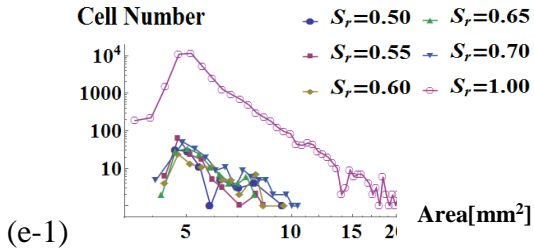
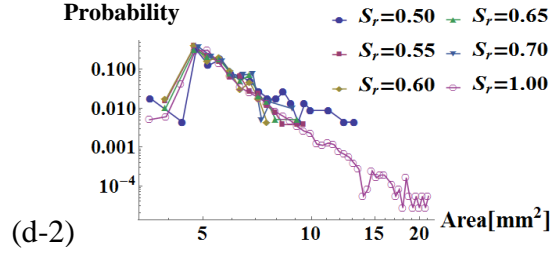
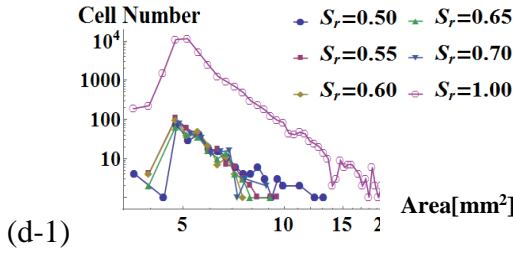
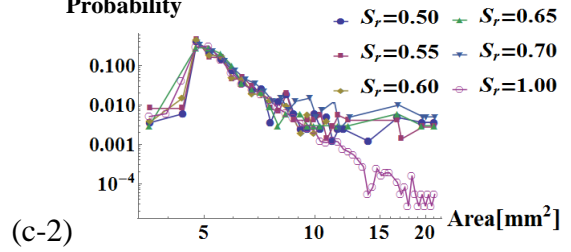
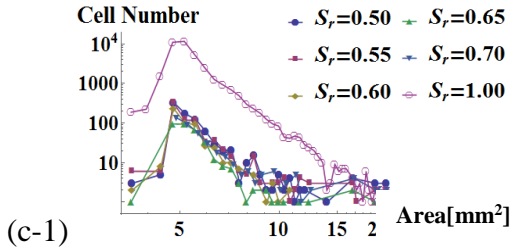
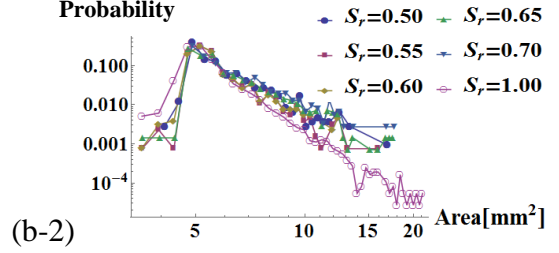
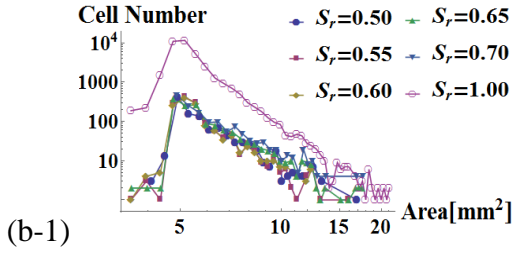
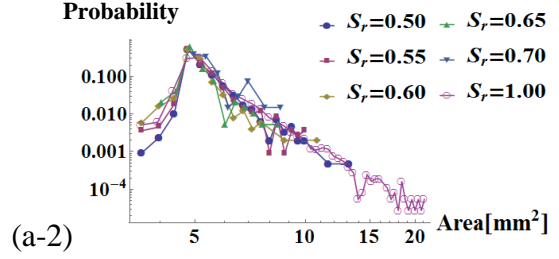


**Fig. 6.3** Wetted Voronoi cell area distributions for six drainage conditions: (a)  $Bo^* = -0.002$ , (b)  $Bo^* = -7.778 \times 10^{-4}$ , (c)  $Bo^* = 0.003$ , (d)  $Bo^* = 0.006$  and (e)  $Bo^* = 0.010$ . The correlated parameters for different drainage conditions refer to the experiments in Table. 3.1.

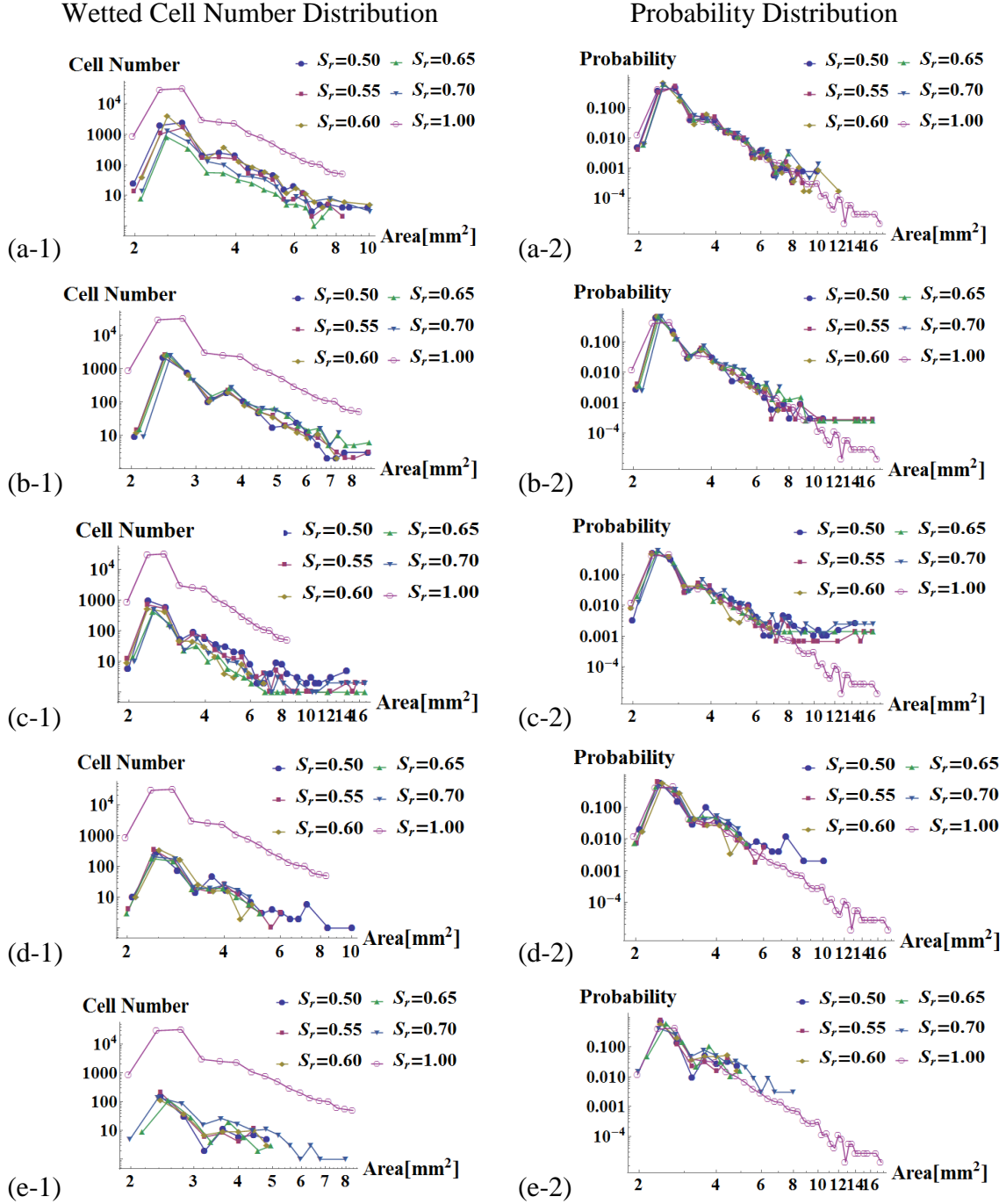


**Fig. 6.4** Wetted Delaunay Triangle (within saturated clusters) area distributions for six drainage conditions: (a)  $Bo^* = -0.002$ , (b)  $Bo^* = -7.778 \times 10^{-4}$ , (c)  $Bo^* = 0.003$ , (d)  $Bo^* = 0.006$  and (e)  $Bo^* = 0.010$ . The correlated parameters for different drainage conditions refer to the experiments in Table. 3.1.

### 6.3 Spatial distribution of wetted cells

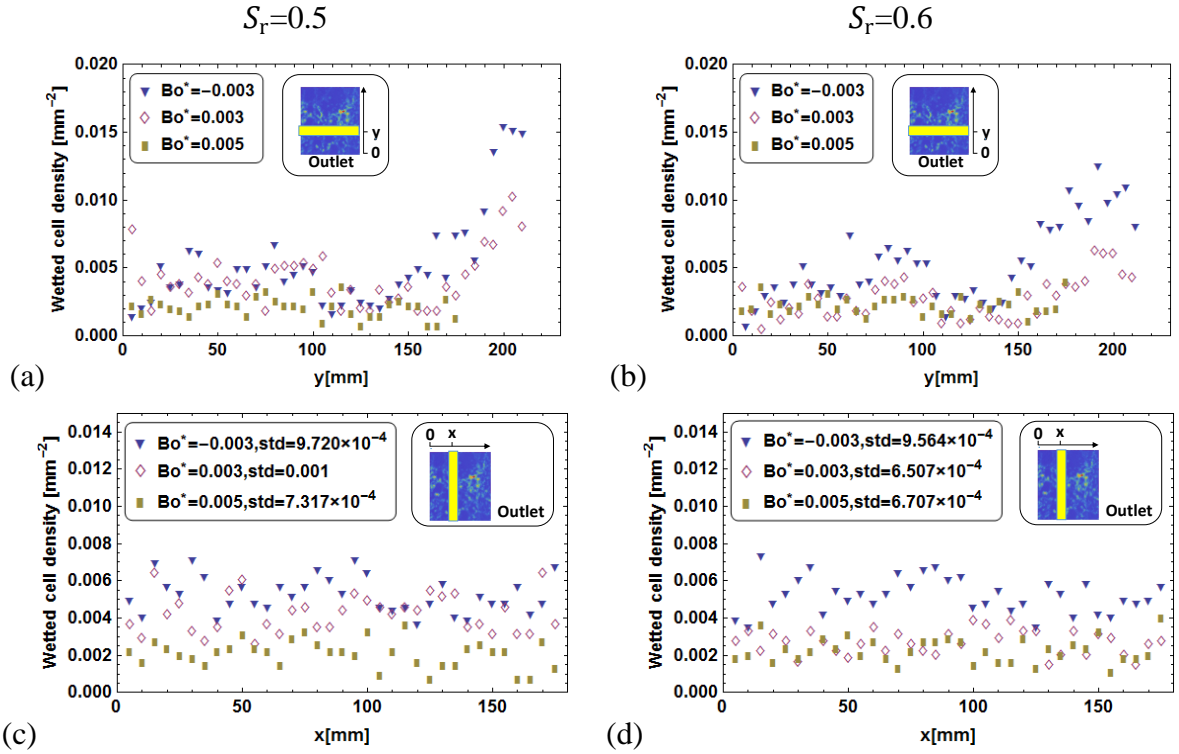


**Fig. 6.5** Histogram showing the spatial distributions of wetted cells in the model for three experiments in a Voronoi mesh. On (a) and (b) we show the wetted cell density inside sub windows in the top-bottom direction for different saturation levels, as a function of the distance  $y$  to the outlet. On the inset we show the orientation of  $y$  axis with respect to the model and a sub window (made  $\approx 4$  times taller than the ones used in our analysis, to aid visualisation). On (c) and (d) we show a similar analysis in the perpendicular direction for different saturation levels. Again, on the inset we show the orientation of  $x$  axis with respect to the model and a sub window (made  $\approx 4$  times wider than the ones used in our analysis, to aid visualisation).

Fig. 6.5 shows the spatial distributions of wetted cell density in two directions of the model for three flow conditions by two saturation levels. These distributions are produced via a histogram of the data with linear binning. The wetted cells of interest in our analysis is those located inside saturated clusters. In Fig. 6.5(a) and (b), we divided the top-bottom distance into 45 equal sub windows (height=5 mm), each one spanning the whole porous medium width. The histogram shows the probability density of wetted cells within each sub windows as a function of  $y$ , the distance between the sub window centre and outlet. This measurement is taken at the

moment when the liquid occupies 50% and 60% of the void space in the porous medium. Apart from the relatively large cells randomly distributed along the model, the distributions are essentially constant for the largest part of the system, with an increase for the sub windows close to the top side of the system. However, experiments with relatively large generalised Bond numbers have a constant probability density of wetted cells along the top-bottom direction, which is reflected in the distribution points in Fig. 6.5. The correlation observed between probability density differences arises from the fact that generalised Bond number defines the stability of displacement structure. What's more, as expected, the probability density of wetted cell tends to 0 for sub windows close to outlet, since that corresponds to the region filled with liquid phase and saturated clusters are only formed in the area mostly occupied by air phase.

Similarly, in Fig. 6.5(c) and Fig. 6.5(d) we divided the perpendicular distance into 36 equal sub windows (width=5 mm), each one spanning the whole porous medium height. The histograms shows the probability density of wetted cells within a sub window on a perpendicular direction. To quantify the amount of variance of our data sets, the standard deviation is computed and shown in the plot legends in Fig. 6.5(c) and Fig. 6.5(d). The low standard deviation for each data set indicates that the distribution is essentially stable, which shows that the boundaries on the  $x$  axis of the model have little effect on the formation of saturated clusters. In addition, as can be seen, the mean values of the wetted cell probability density decrease as the generalised Bond number increases, which follows the results in last chapter: compared with stable liquid front, unstable displacement structure can generate more saturated clusters at the same saturation level.

As can be seen in Fig. 6.5, the histograms in the first column have the higher probability density than the histograms in the second column for the same sub windows in both directions, i.e., the lower saturation level has more wetted cells than the high saturation level at the same region in the model. This is due to the removing the largest wet area in the process.

## 6.4 Discussion

We have presented a detailed pore-scale analysis of the influence of pore structure on the distribution of saturated clusters in micromodels. The geometries we have considered consist of quasi two-dimensional porous medium (a modified Hele-Shaw cell), constructed by glass beads with homogeneous grain size. By randomly fully packed our porous medium, some crystallised and non-crystallised region are constructed in our model.

Our results provide a deep understanding of the distribution of trapped water in random close packings of spheres concentrating on two-phase flow in porous media, which can serve as a basis for models of multiphase flows in the oil industry. In oil industry, the invading liquid is oil and defending liquid is water, representing the primary oil migration into the reservoir. This invasion percolation process can be represented by the model used in our experiment. By knowing how the pore-structure is packed, the water-wet or oil-wet cell distribution can then be computed. The distribution of either water-wet cluster or oil-wet cluster has a direct influence of the relative permeability on both liquids [12, 72]. In this case, it is important to allocate the positions of both water-wet and oil-wet clusters in designing oil recovery schemes. Our results can give a potential solution for this topic.

In addition, in pore-level modelling of multiphase flow in porous media, the pore-size distribution has great effect upon the residual saturation [73]. The pore-size distribution, can be computed from the cell-size distribution by removing the projection area of an individual solid grain in our study. The correlated wetted cell-size distribution can then be interpreted by the knowing cell-size distribution of the porous medium.

## **6.5 Summary**

In this chapter, we first built up an algorithm to quantify the wetted cells in both Voronoi and Delaunay tessellation under different drainage conditions. We then analysed the wetted cell spatial and temporal distributions for multiple cases. It is concluded that the cell-size distribution of the porous medium can directly determine the wetted cell size probability distribution for all cases. Moreover, by comparing the wetted cell distribution in both directions, boundary effects could be neglected.

# Chapter 7

## Conclusion

In this study we experimentally evaluated the formation of temporarily entrapped liquid phase and its subsequent evolution during drainage processes of wetted granular materials. The system allows tuning of gravity by changing the tilt angle of the container and applying various withdrawal rates. In a drainage process, the unsaturated zone can be separated into two regions: a continuous saturated zone with a fast draining rate under the rapid moving front and a discontinuous saturated zone where the liquid is viscous delayed. The discontinuous entrapped liquid phase is defined as saturated clusters. The observed saturated clusters are determined by the dominance of viscous force, i.e., viscous and its evolution are statistically quantified, depending on porous medium properties and applied drainage rates. In addition, we compared the accumulated saturated cluster area for different scenarios and realized that the fraction of viscous limited pore bodies depends on the hydraulic resistive liquid phase is held in poorly connected pore clusters and small pore bodies due to the fact that gravitational force cannot balance the effect of viscous force. The saturated cluster size distribution properties of the porous medium.

The main conclusions are as follows:

1. The experimental results of the morphological characteristics of the displacement front are in agreement with the criteria from literature: when the flow rate converges to the saturated hydraulic conductivity, the observed liquid front become unstable and viscous fingers are formed; when the flow rate is small, the liquid front is observed as a plateau in the porous medium. At high flow rates, the experiment data revealed the trend that the accumulated water content entrapped behind the displacement front increase with increasing drainage flow rates because more liquid phase is viscous limited. These results could serve as a theoretical basis for a better interpretation of relative permeability and mass transfer in porous media.
2. The distribution of saturated clusters is found to follow a lognormal distribution. It is concluded that the scale parameter  $\mu$  and shape parameter  $\sigma$  negatively and positively

correlate with  $Bo^*$ , respectively. Due to the fact that a strong linear dependence exists between lognormal distribution parameters and generalised Bond number,  $Bo^*$ , it is possible to generate a function containing  $\mu$ ,  $\sigma$  and  $Bo^*$  for describing the cluster distribution at various saturation levels. Knowing this, combined with the total surface energy calculated by the area of interfaces, it is possible to include this additional grain-scale information in constitutive modelling of unsaturated soils using both the degree of saturation and generalised Bond number,  $Bo^*$ .

3. The pore-scale structure has a strong positive influence on spatial extent of viscous delayed pores during a multiphase flow. The wetted cell size probability curve perfectly follows the global-scale cell size probability curve. Furthermore, according to the systematic analysis of the fraction of wetted cell in two perpendicular directions, the boundary effect on the distribution of wetted cells could be neglected. This means that our results can be applied into infinite two-dimensional systems, which could support the theoretical framework for three dimensional porous media.

This study gives a comprehensive investigation of pore-scale analysis of viscous limited regions of multiphase flow in porous media. Experimental results from a two phase flow in a randomly constructed 2-D sphere system indicate the effects of both pore-structure and drainage conditions on the spatial information of viscous restricted patches. With tuning network model parameters to match the data or dependent on explicit description of disordered three dimensional network, conclusions extracted from this study could be applied into a variety of situations in realistic geological scenarios, including the effects of two or three phase flow and the influence of flow rate on residual oil saturation in oil recovery.

# References

- [1] A. Szymkiewicz, *Modelling water flow in unsaturated porous media: accounting for nonlinear permeability and material heterogeneity*: Springer Science & Business Media, 2012.
- [2] W. J. Likos, "Effective Stress in Unsaturated Soil: Accounting for Surface Tension and Interfacial Area," *Vadose Zone Journal*, vol. 13, 2014.
- [3] Y. Yuan and T. R. Lee, "Contact Angle and Wetting Properties," in *Surface Science Techniques*, G. Bracco and B. Holst, Eds., ed Berlin, Heidelberg: Springer Berlin Heidelberg, 2013, pp. 3-34.
- [4] Y. Méheust, G. Løvoll, K. J. Måløy, and J. Schmittbuhl, "Interface scaling in a two-dimensional porous medium under combined viscous, gravity, and capillary effects," *Physical Review E*, vol. 66, p. 051603, 11/11/ 2002.
- [5] F. Hoogland, P. Lehmann, and D. Or, "The formation of viscous limited saturation zones behind rapid drainage fronts in porous media," *Water Resources Research*, vol. 51, pp. 9862-9890, 2015.
- [6] B. H. Kueper and E. O. Frind, "An overview of immiscible fingering in porous media," *Journal of Contaminant Hydrology*, vol. 2, pp. 95-110, 1988/03/01 1988.
- [7] T. Saba and T. H. Illangasekare, "Effect of groundwater flow dimensionality on mass transfer from entrapped nonaqueous phase liquid contaminants," *Water Resources Research*, vol. 36, pp. 971-979, 2000.
- [8] C. T. Simmons, K. A. Narayan, and R. A. Wooding, "On a test case for density-dependent groundwater flow and solute transport models: The Salt Lake Problem," *Water Resources Research*, vol. 35, pp. 3607-3620, 1999.
- [9] H. Auradou, K. J. Måløy, J. Schmittbuhl, A. Hansen, and D. Bideau, "Competition between correlated buoyancy and uncorrelated capillary effects during drainage," *Physical Review E*, vol. 60, pp. 7224-7234, 12/01/ 1999.
- [10] T. Podgorski, J. M. Flesselles, and L. Limat, "Corners, Cusps, and Pearls in Running Drops," *Physical Review Letters*, vol. 87, p. 036102, 06/27/ 2001.
- [11] G. W. Su, J. T. Geller, J. R. Hunt, and K. Pruess, "Small-Scale Features of Gravity-Driven Flow in Unsaturated Fractures," *Vadose Zone Journal*, vol. 3, pp. 592-601, 2004.
- [12] M. J. Blunt, M. D. Jackson, M. Piri, and P. H. Valvatne, "Detailed physics, predictive capabilities and macroscopic consequences for pore-network models of multiphase flow," *Advances in Water Resources*, vol. 25, pp. 1069-1089, 8// 2002.
- [13] D. Wildenschild, J. Hopmans, M. Rivers, and A. Kent, "Quantitative analysis of flow processes in a sand using synchrotron-based X-ray microtomography," *Vadose Zone Journal*, vol. 4, pp. 112-126, 2005.
- [14] G. Løvoll, M. Jankov, K. J. Måløy, R. Toussaint, J. Schmittbuhl, G. Schäfer, *et al.*, "Influence of Viscous Fingering on Dynamic Saturation-Pressure Curves in Porous Media," *Transport in Porous Media*, vol. 86, pp. 305-324, 2011.
- [15] R. Finn, "Capillary surface interfaces," *Notices AMS*, vol. 46, pp. 770-781, 1999.
- [16] T. Young, "An Essay on the Cohesion of Fluids," *Philosophical Transactions of the Royal Society of London*, vol. 95, pp. 65-87, January 1, 1805 1805.
- [17] T. Chen, M.-S. Chiu, and C.-N. Weng, "Derivation of the generalized Young-Laplace equation of curved interfaces in nanoscaled solids," *Journal of Applied Physics*, vol. 100, p. 074308, 2006.

- [18] P. d. Laplace, P. Laplace, M. Laplace, M. Le Marquis de Laplace, N. Bowditch, A. Young, *et al.*, "Traité de mécanique céleste," ed: JSTOR, 1839.
- [19] F. Moebius and D. Or, "Pore scale dynamics underlying the motion of drainage fronts in porous media," *Water Resources Research*, vol. 50, pp. 8441-8457, 2014.
- [20] F. Moebius and D. Or, "Interfacial jumps and pressure bursts during fluid displacement in interacting irregular capillaries," *Journal of Colloid and Interface Science*, vol. 377, pp. 406-415, 7/1/ 2012.
- [21] P. Lehmann, S. Assouline, and D. Or, "Characteristic lengths affecting evaporative drying of porous media," *Physical Review E*, vol. 77, p. 16, May 2008.
- [22] M. Moura, E. A. Fiorentino, K. J. Måløy, G. Schäfer, and R. Toussaint, "Impact of sample geometry on the measurement of pressure-saturation curves: Experiments and simulations," *Water Resources Research*, vol. 51, pp. 8900-8926, 2015.
- [23] N. Mitarai and F. Nori, "Wet granular materials," *Advances in Physics*, vol. 55, pp. 1-45, 2006.
- [24] K. Al-Fossail and L. L. Handy, "Correlation between capillary number and residual water saturation," *Journal of Colloid and Interface Science*, vol. 134, pp. 256-263, 1990/01/01 1990.
- [25] N. J. Alvarez, L. M. Walker, and S. L. Anna, "A non-gradient based algorithm for the determination of surface tension from a pendant drop: Application to low Bond number drop shapes," *Journal of Colloid and Interface Science*, vol. 333, pp. 557-562, 5/15/ 2009.
- [26] A. Birovljev, L. Furuberg, J. Feder, T. Jssang, K. J. Mly, and A. Aharony, "Gravity invasion percolation in two dimensions: Experiment and simulation," *Physical Review Letters*, vol. 67, pp. 584-587, 07/29/ 1991.
- [27] S. M. P. Blom and J. Hagoort, "How to Include the Capillary Number in Gas Condensate Relative Permeability Functions?."
- [28] E. T. Gawlinski and H. E. Stanley, "Continuum percolation in two dimensions: Monte Carlo tests of scaling and universality for non-interacting discs," *Journal of Physics A: Mathematical and General*, vol. 14, p. L291, 1981.
- [29] D. Or, "Scaling of capillary, gravity and viscous forces affecting flow morphology in unsaturated porous media," *Advances in Water Resources*, vol. 31, pp. 1129-1136, 9// 2008.
- [30] D. J. Crisp and R. Williams, "Direct measurement of pore-size distribution on artificial and natural deposits and prediction of pore space accessible to interstitial organisms," *Marine Biology*, vol. 10, pp. 214-226, 1971.
- [31] D. G. Fredlund and H. Rahardjo, *Soil mechanics for unsaturated soils*: John Wiley & Sons, 1993.
- [32] N. Lu, J. W. Godt, and D. T. Wu, "A closed-form equation for effective stress in unsaturated soil," *Water Resources Research*, vol. 46, pp. n/a-n/a, 2010.
- [33] N. Lu and W. J. Likos, "Suction stress characteristic curve for unsaturated soil," *Journal of geotechnical and geoenvironmental engineering*, vol. 132, pp. 131-142, 2006.
- [34] W. J. Likos and N. Lu, "Unsaturated soil mechanics," ed: John Wiley and Sons Inc., New Jersey, 2004.
- [35] W. J. Likos and N. Lu, "Hysteresis of capillary stress in unsaturated granular soil," *Journal of Engineering mechanics*, vol. 130, pp. 646-655, 2004.
- [36] N. Lu, T.-H. Kim, S. Sture, and W. J. Likos, "Tensile strength of unsaturated sand," *Journal of engineering mechanics*, vol. 135, pp. 1410-1419, 2009.
- [37] S. Horseman, J. Harrington, and P. Sellin, "Gas migration in KBS-3 buffer bentonite: sensitivity of test parameters to experimental boundary conditions."

- [38] J. Gottlieb and P. Dietrich, "Identification of the permeability distribution in soil by hydraulic tomography," *Inverse Problems*, vol. 11, p. 353, 1995.
- [39] G. C. Tzimas, T. Matsuura, D. G. Avraam, W. Van der Bruggen, G. N. Constantinides, and A. C. Payatakes, "The Combined Effect of the Viscosity Ratio and the Wettability during Forced Imbibition through Nonplanar Porous Media," *Journal of Colloid and Interface Science*, vol. 189, pp. 27-36, 5/1/ 1997.
- [40] S. K. Vanapalli, M. V. Nicotera, and R. S. Sharma, "Axis Translation and Negative Water Column Techniques for Suction Control," in *Laboratory and Field Testing of Unsaturated Soils*, A. Tarantino, E. Romero, and Y.-J. Cui, Eds., ed Dordrecht: Springer Netherlands, 2009, pp. 33-48.
- [41] O. Vizika, D. G. Avraam, and A. C. Payatakes, "On the Role of the Viscosity Ratio during Low-Capillary-Number Forced Imbibition in Porous Media," *Journal of Colloid and Interface Science*, vol. 165, pp. 386-401, 1994/07/01 1994.
- [42] J. Wang and M. Dong, "Trapping of the non-wetting phase in an interacting triangular tube bundle model," *Chemical Engineering Science*, vol. 66, pp. 250-259, 2/1/ 2011.
- [43] P. Yin and G.-F. Zhao, "Numerical study of two-phase fluid distributions in fractured porous media," *International Journal for Numerical and Analytical Methods in Geomechanics*, vol. 39, pp. 1188-1211, 2015.
- [44] J. Gouyet, M. Rosso, and B. Sapoval, "Fractal structure of diffusion and invasion fronts in three-dimensional lattices through the gradient percolation approach," *Physical review. B, Condensed matter*, vol. 37, p. 1832, 1988.
- [45] M. Long and F. Peng, "A Box-Counting Method with Adaptable Box Height for Measuring the Fractal Feature of Images," *Radioengineering*, 2013.
- [46] A. Conci and C. B. Proença, "A fractal image analysis system for fabric inspection based on a box-counting method," *Computer Networks and ISDN Systems*, vol. 30, pp. 1887-1895, 11/12/ 1998.
- [47] J. Li, Q. Du, and C. Sun, "An improved box-counting method for image fractal dimension estimation," *Pattern Recognition*, vol. 42, pp. 2460-2469, 11// 2009.
- [48] K. Foroutan-pour, P. Dutilleul, and D. L. Smith, "Advances in the implementation of the box-counting method of fractal dimension estimation," *Applied Mathematics and Computation*, vol. 105, pp. 195-210, 11// 1999.
- [49] A. K. Bisoi and J. Mishra, "On calculation of fractal dimension of images," *Pattern Recognition Letters*, vol. 22, pp. 631-637, 5// 2001.
- [50] S. Buczkowski, P. Hildgen, and L. Cartilier, "Measurements of fractal dimension by box-counting: a critical analysis of data scatter," *Physica A: Statistical Mechanics and its Applications*, vol. 252, pp. 23-34, 4/1/ 1998.
- [51] S. Buczkowski, S. Kyriacos, F. Nekka, and L. Cartilier, "The modified box-counting method: Analysis of some characteristic parameters," *Pattern Recognition*, vol. 31, pp. 411-418, 4// 1998.
- [52] X. C. Jin, S. H. Ong, and Jayasooriah, "A practical method for estimating fractal dimension," *Pattern Recognition Letters*, vol. 16, pp. 457-464, 5// 1995.
- [53] N. Sarkar and B. B. Chaudhuri, "An efficient approach to estimate fractal dimension of textural images," *Pattern Recognition*, vol. 25, pp. 1035-1041, 1992.
- [54] M. D. Fredlund, D. G. Fredlund, and G. Wilson, "Prediction of the soil-water characteristic curve from grain-size distribution and volume-mass properties," in *Proc., 3rd Brazilian Symp. on Unsaturated Soils*, 1997, pp. 13-23.
- [55] J. Bear, *Dynamics of fluids in porous media*: Courier Corporation, 2013.
- [56] Y. Gan, F. Maggi, G. Buscarnera, and I. Einav, "A particle–water based model for water retention hysteresis," *Géotechnique Letters*, vol. 3, pp. 152-161, 2013.

- [57] G. Løvoll, Y. Méheust, R. Toussaint, J. Schmittbuhl, and K. J. Måløy, "Growth activity during fingering in a porous Hele-Shaw cell," *Physical Review E*, vol. 70, p. 026301, 08/09/ 2004.
- [58] N. Shokri, P. Lehmann, P. Vontobel, and D. Or, "Drying front and water content dynamics during evaporation from sand delineated by neutron radiography," *Water Resources Research*, vol. 44, pp. n/a-n/a, 2008.
- [59] J.-F. Bruchon, J.-M. Pereira, M. Vandamme, N. Lenoir, P. Delage, and M. Bornert, "Full 3D investigation and characterisation of capillary collapse of a loose unsaturated sand using X-ray CT," *Granular Matter*, vol. 15, pp. 783-800, 2013.
- [60] A. E. Scheidegger, "The Physics of Flow Through Porous Media," *Soil Science*, vol. 86, p. 355, 1958.
- [61] J. Aitchison and J. A. C. Brown, *The lognormal distribution* vol. 5: CUP Archive, 1976.
- [62] I. J. Myung, "Tutorial on maximum likelihood estimation," *Journal of mathematical Psychology*, vol. 47, pp. 90-100, 2003.
- [63] B. F. Ginos, "Parameter estimation for the lognormal distribution," 2009.
- [64] J. Lee Rodgers and W. A. Nicewander, "Thirteen Ways to Look at the Correlation Coefficient," *The American Statistician*, vol. 42, pp. 59-66, 1988/02/01 1988.
- [65] S. Fordham, "On the Calculation of Surface Tension from Measurements of Pendant Drops," *Proceedings of the Royal Society of London. Series A. Mathematical and Physical Sciences*, vol. 194, pp. 1-16, 1948.
- [66] J. M. Andreas, E. A. Hauser, and W. B. Tucker, "BOUNDARY TENSION BY PENDANT DROPS1," *The Journal of Physical Chemistry*, vol. 42, pp. 1001-1019, 1937/01/01 1937.
- [67] J. D. Berry, M. J. Neeson, R. R. Dagastine, D. Y. Chan, and R. F. Tabor, "Measurement of surface and interfacial tension using pendant drop tensiometry," *Journal of colloid and interface science*, vol. 454, pp. 226-237, 2015.
- [68] K. L. Mittal, "Contact Angle, Wettability and Adhesion, Volume 4," ed: VSP - An imprint of BRILL.
- [69] C. Clegg, *Contact Angle Made Easy*: Carl Clegg, 2013.
- [70] C. W. Macosko and R. G. Larson, "Rheology: principles, measurements, and applications," 1994.
- [71] H.-f. Xu and K.-h. Xie, "Effective stress in soils under different saturation conditions," *Journal of Central South University of Technology*, vol. 18, pp. 2137-2142, 2011.
- [72] M. J. Blunt, "Flow in porous media — pore-network models and multiphase flow," *Current Opinion in Colloid & Interface Science*, vol. 6, pp. 197-207, 6// 2001.
- [73] G. R. Jerauld and S. J. Salter, "The effect of pore-structure on hysteresis in relative permeability and capillary pressure: Pore-level modeling," *Transport in Porous Media*, vol. 5, pp. 103-151, April 01 1990.

# Appendix A:

## Image processing

The data analysis of the image series recorded with the digital camera was accomplished using a code that implemented the following procedure:

1. The boundaries of the image were first trimmed. And the images were then converted from an RGB format to the binary format (liquid phase 0, air phase 1), using the thresholds adapted for each experiment.
2. Small connected components ( $< \pi \text{ mm}^2$ ) in a binary image were then replaced with background pixels.
3. Similarly, small connected components were removed again after negating all colours in the binary.
4. An array was computed in which each pixel of the image was replaced by an integer index representing the connected foreground image component in which the pixel lies. This was obtained by applying the 4-connectivity connected-component labelling algorithm to the individual image.
5. The areas identified were converted into a data set using the known resolution of the images.

The specific program is written below:

```
SetDirectory[NotebookDirectory[]]
ClearAll;
files = FileNames["*.JPG", {"1 ml inject 1st"}];
nfile = Length[files]; nfile = 2;
data = Table[Import[files[[j]]], {j, 1, nfile}];
smallSize = 190;
i = 1;

window[list_, {xmin_, xmax_}] := Pick[list, Boole[xmin ≤ # ≤ xmax] & /@ list, 1]
```

```

Do[{img = ImageResize[Import[files[[i]], {1500, 1000}];
  img = ImageTrim[img, {{0, 0}, {1, 1}}, DataRange → {{0, 1}, {0, 1}}]; le
  img1 = DeleteSmallComponents[Binarize[img], smallSize];
  img1 = DeleteSmallComponents[ColorNegate[img1], smallSize];
  img1 = ColorNegate[Binarize[img1]];
  (*markers=DeleteSmallComponents[MaxDetect[GaussianFilter[img1,3],Padding→1],smallSize];
  img1=Closing[GeodesicDilation[markers,img1],DiskMatrix[3]];*)
  img2 = MorphologicalComponents[img1] // Colorize;
  img3 = WatershedComponents[img1, Method → {"MinimumSaliency", 2.0}] // Colorize;
  img4 = ColorNegate[img1];

  img5 = MorphologicalComponents[img4] // Colorize;
  img6 = WatershedComponents[img4, Method → {"MinimumSaliency", 1.0}] // Colorize;
  (*image processing*)

  data1 = Tally[Flatten[MorphologicalComponents[img5, CornerNeighbors → False]]];
  d = window[data1[[All, 2]], {10, 4000}];
  {binsL, countsL} = HistogramList[Sqrt[d], {5}];
  dataL[i] = Transpose@{Flatten[{Rest[binsL] + Most[binsL]}/11.0], Flatten[countsL]};
  (*liquid data*)
  data2 = Tally[Flatten[MorphologicalComponents[img2, CornerNeighbors → False]]];
  d = window[data2[[All, 2]], {10, 3500}];
  {binsA, countsA} = HistogramList[Sqrt[d], {5}];
  dataA[i] = Transpose@{Flatten[{Rest[binsA] + Most[binsA]}/11.0], Flatten[countsA]};
  (*air data*)
  , {i, 1, nfile}}

PlotOptions = {Frame → True, Axes → {True, False}, Filling → Axis, FrameTicks → All,
  PlotRangePadding → .2, PlotRange → All, PlotLegends → files, ImageSize → 300,
  FrameLabel → {"Size(mm)", "Number"}};
GraphicsGrid[{{ListLinePlot[Table[dataL[i], {i, 1, nfile}], PlotOptions, PlotLabel →
  "Saturated Cluster Distribution"},
ListLinePlot[Table[dataA[i], {i, 1, nfile}], PlotOptions,
  PlotLabel → "Air Cluster Distribution"]}]}

```

# Appendix B:

## Maximum likelihood estimation

In this appendix section, the maximum likelihood method used in our data fitting is introduced. Maximum likelihood method is the procedure of finding the value of one or more parameters for a given statistic which makes the known likelihood distribution a maximum.

```
(*Lognormal*)
ClearAll["Global`*"]
$HistoryLength = 0;
SetDirectory[NotebookDirectory[]];
stream = OpenRead["0.5-dr-0du20ml.dat"];
(*cluster area/liquid base*)
binWidth = 2.5;
Data1 = Flatten[ReadList[stream, {Number}] / 30.0]; (*pixel number to mm2*)
Data1 = Drop[Sort[Data1, #1 < #2 &], -5]; (*delete fully saturated region in each image*)
Data1s = Data1 -  $\pi$ ; (*shift data for goodness test*)
PDF1 = BinCounts[Data1, binWidth]; (*gather data with binwidth 2.5mm2*)
PDF1 = PDF1 / Length[Data1]; (*sum of binlist number/all number*)
CDF1 = Accumulate[PDF1];
PDF1 = PDF1 / binWidth;
(*shift data*)
xmin = Min[Data1] + binWidth / 2 -  $\pi$ ;
xmax = Times[Length[PDF1], binWidth] + binWidth / 2 -  $\pi$ ;
x1 = Table[p, {p, xmin, xmax + binWidth, binWidth}];

Dist1P = Transpose[{x1, PDF1}];
Dist1 = Transpose[{x1, CDF1}];
Para1 = FindFit[Dist1, CDF[LogNormalDistribution[ $\mu$ ,  $\sigma$ ], x], { $\mu$ ,  $\sigma$ }, x];
Dist1 = Transpose[{x1, CDF1}];
Para1 = FindFit[Dist1,
  CDF[LogNormalDistribution[ $\mu$ ,  $\sigma$ ], x], { $\mu$ ,  $\sigma$ },
  x];
```

```

lf[data_, μ_, σ_] := Times @@ (PDF[LogNormalDistribution[μ, σ], #] & /@ data)
Eqs[Data_] := {∂μ lf[Data, μ, σ] == 0, ∂σ lf[Data, μ, σ] == 0};

```

```

Soll = FindRoot[Eqs[Data1], {{μ, Para1[[1, 2]]}, {σ, Para1[[2, 2]]}}, PrecisionGoal → 1]

```

(\*shift back both data and curve\*)

```

xmin1 = Min[Data1] + binWidth / 2;
xmax1 = Times[Length[PDF1], binWidth] + binWidth / 2;
x11 = Table[p, {p, xmin1, xmax1 + binWidth, binWidth}];
Dist1P = Transpose[{x11, PDF1}];
y11 = Flatten[Table[{PDF[LogNormalDistribution[μ, σ], x] /. Soll}, {x, xmin, xmax +
    binWidth, binWidth}]];
Dist1PMLE = Transpose[{x11, y11}];
PlotOptions = {Frame → True, PlotMarkers → {■, 13}, FrameStyle → Directive[Black, Bold],
    Axes → {True, False}, AxesOrigin → {2, 0}, FrameTicks → All, Joined → {False, True},
    PlotLegends → Placed[SwatchLegend[{"Experimental Data", "MLE"}, LegendMarkers →
        {■, "Line"}], {{0.68, 0.70}, {0.5, 0.1}}, ImageSize → 300, FrameLabel →
        {"Area[mm2", "PDF"}], LabelStyle → Directive[Black, Bold, 15]};
plot1 = ListLogLinearPlot[Dist1P, PlotOptions];
plot2 = LogLinearPlot[PDF[LogNormalDistribution[0.28, 2.46], x - π] // Evaluate, {x, 3, 50},
    Filling → Axis, PlotRange → {0, .3}, Frame → True, FrameStyle → Directive[Black, Bold],
    FrameLabel → {"Area [mm2", "PDF"}, PlotLegends →
        Placed[SwatchLegend[{"MLE-lognormal Fitting"}, LegendMarkers → {"Line", ■}],
        {{0.68, 0.80}, {0.5, 0.1}}, LabelStyle → Directive[Black, Bold, 13]];
Show[{plot2, plot1}]

```

# Appendix C:

## Lognormal parameters

In last section, we illustrated a statistical method of estimating the parameters of a statistical model given observation. To find the relationship of the correlation of the fitting parameters and the dimensionless number used in our study, we used correlation coefficient to quantify their dependence.

```
ClearAll["Global`*"]
$HistoryLength = 0;
SetDirectory[NotebookDirectory[]]
data = Import[NotebookDirectory[] <> "Sr diff horizontal.xlsx"][[6]];
axisx = Flatten[Transpose[data][[13]][[1 ;; 11]]];

axisy[1] = Flatten[Transpose[data][[15]][[1 ;; 11]]];
axisy[2] = Flatten[Transpose[data][[16]][[1 ;; 11]]];
axisy[3] = Flatten[Transpose[data][[17]][[1 ;; 11]]];
axisy[4] = Flatten[Transpose[data][[18]][[1 ;; 11]]];
axisy[5] = Flatten[Transpose[data][[19]][[1 ;; 11]]];

axisy[6] = Flatten[Transpose[data][[20]][[1 ;; 11]]];
axisy[7] = Flatten[Transpose[data][[21]][[1 ;; 11]]];
axisy[8] = Flatten[Transpose[data][[22]][[1 ;; 11]]];
axisy[9] = Flatten[Transpose[data][[23]][[1 ;; 11]]];
axisy[10] = Flatten[Transpose[data][[24]][[1 ;; 11]]];

axisy[11] = Flatten[Transpose[data][[14]][[1 ;; 11]]];
axisy[12] = Flatten[Transpose[data][[25]][[1 ;; 11]]];

Im1 = LinearModelFit[Thread[{axisx, axisy[11]}], x, x];
Im2 = LinearModelFit[Thread[{axisx, axisy[12]}], x, x];
```

```

option = {Mesh → All, Frame → True, FrameStyle → Directive[Black, Bold],
  PlotMarkers → {■, 18}, PlotStyle → ColorData[97, "ColorList"],
  LabelStyle → Directive[Black, FontSize → 12, AbsoluteThickness[1.6]],
  TicksStyle → Directive[FontSize → 16]};
plot1 = Show[ListPlot[Table[Thread[{{axisx, axisy[i]}], {i, 1, 5}], option,
  FrameLabel → {"Bo*", "μ"}, PlotLegends →
  Placed[SwatchLegend[{"Sr=0.50", "Sr=0.55", "Sr=0.60", "Sr=0.65", "Sr=0.70"},
  LegendFunction → "Frame", LegendMarkers → Automatic, LabelStyle →
  Directive[Bold, FontSize → 12]], {{0.78, 0.16}, {0.1, 0.1}}]],
  Plot[Im1[x], {x, -1, 5}, PlotStyle → {Dashed, Blue, Thickness[0.015]}]]
plot2 = Show[ListPlot[Table[Thread[{{axisx, axisy[j]}], {j, 6, 10}], option,
  FrameLabel → {"Bo*", "σ"}, PlotLegends →
  Placed[SwatchLegend[{"Sr=0.50", "Sr=0.55", "Sr=0.60", "Sr=0.65", "Sr=0.70"},
  LegendFunction → "Frame", LegendMarkers → Automatic, LabelStyle →
  Directive[Bold, FontSize → 12]], {{0.78, 0.06}, {0.1, 0.1}}]],
  Plot[Im2[x], {x, -1, 5}, PlotStyle → {Dashed, Red, Thickness[0.015]}]]

```

# Appendix D:

## Wetted cell distribution

In Fig. 6.3 and Fig. 6.4, we have shown the wetted cell number and probability distribution from both Voronoi and Delaunay meshes. In this section, we give a specific example of wetted cell number distribution of Voronoi mesh.

```
ClearAll["Global`*"];
$HistoryLength = 0;
SetDirectory["G:\\11-22\\"];
data = Flatten[Table[Import["G:\\11-22\\IMGareacell_"
    <> ToString[i] <> ".csv", "Data"], {i, 5}]];

{bins, counts} = HistogramList[data, {Min[data], Max[data], 0.4}];
counts = N[Function[x, x/Total[counts]]/@ counts];
total = {Drop[bins, 1], counts} // Transpose;
total = Select[total, #[[2]] > 0 &];

data5 = Table[Import["G:\\some other exep\\5ml10du\\0.5-dr-10du5ml\\
0.5-dr-10du5mlclusterdw_" <> ToString[i] <> ".csv", "Data"], {i, 5}];
data5 = Sort[Flatten[data5, 1], #1[[1]] < #2[[1]] &];
binwidth = 0.4;
data5 = Select[data5, #[[2]] > 0 &];
data5 = data5[[All, 1]];
L = Length[data5];
{bins, counts} = HistogramList[data5, {Min[data5], Max[data5], binwidth}];
counts = N[Function[x, x/L]/@ counts];
data5 = {Drop[bins, 1], counts} // Transpose;
data5 = Select[data5, #[[2]] > 0 &];

data7 = Table[Import["G:\\some other exep\\5ml10du\\0.7-dr-10du5ml\\
0.7-dr-10du5mlclusterdw_" <> ToString[i] <> ".csv", "Data"], {i, 5}];
```

```

data7 = Sort[Flatten[data7, 1], #1[[1]] < #2[[1]] &];
binwidth = 0.4;
data7 = Select[data7, #[[2]] > 0 &];
data7 = data7[[All, 1]];
L = Length[data7];
{bins, counts} = HistogramList[data7, {Min[data7], Max[data7], binwidth}];
counts = N[Function[x, x/L] /@ counts];
data7 = {Drop[bins, 1], counts} // Transpose;
data7 = Select[data7, #[[2]] > 0 &];

```

```

data6 = Table[Import["G:\some other exep\5ml10du\0.60-dr-10du5ml\
0.60-dr-10du5mlclusterdw_" <> ToString[i] <> ".csv", "Data"], {i, 5}];
data6 = Sort[Flatten[data6, 1], #1[[1]] < #2[[1]] &];
binwidth = 0.4;
data6 = Select[data6, #[[2]] > 0 &];
data6 = data6[[All, 1]];
L = Length[data6];
{bins, counts} = HistogramList[data6, {Min[data6], Max[data6], binwidth}];
counts = N[Function[x, x/L] /@ counts];
data6 = {Drop[bins, 1], counts} // Transpose;
data6 = Select[data6, #[[2]] > 0 &];

```

```

data55 = Table[Import["G:\some other exep\5ml10du\0.55-dr-10du5ml\
0.55-dr-10du5mlclusterdw_" <> ToString[i] <> ".csv", "Data"], {i, 5}];
data55 = Sort[Flatten[data55, 1], #1[[1]] < #2[[1]] &];
binwidth = 0.4;
data55 = Select[data55, #[[2]] > 0 &];
data55 = data55[[All, 1]];
L = Length[data55];
{bins, counts} = HistogramList[data55, {Min[data55], Max[data55], binwidth}];
counts = N[Function[x, x/L] /@ counts];
data55 = {Drop[bins, 1], counts} // Transpose;
data55 = Select[data55, #[[2]] > 0 &];

```

```

data65 = Table[Import["G:\some other exep\5ml10du\0.65-dr-10du5ml\
0.65-dr-10du5mlclusterdw_" <> ToString[i] <> ".csv", "Data"], {i, 5}];

```

```

data65 = Sort[Flatten[data65, 1], #1[[1]] < #2[[1]] &];
binwidth = 0.4;
data65 = Select[data65, #[[2]] > 0 &];
data65 = data65[[All, 1]];
L = Length[data65];
{bins, counts} = HistogramList[data65, {Min[data65], Max[data65], binwidth}];
counts = N[Function[x, x/L] /@ counts];
data65 = {Drop[bins, 1], counts} // Transpose;
data65 = Select[data65, #[[2]] > 0 &];

option = {PlotLegends → {"Sr=0.50", "Sr=0.55", "Sr=0.60", "Sr=0.65", "Sr=0.70",
    "Sr=1.00"}, LabelStyle → Directive[Black, Bold, 30, FontFamily →
    "Times New Roman"], PlotRange → All, LabelStyle → Directive[Black,
    Bold, FontFamily → "Times New Roman"], ImageSize → {600, 400},
    AxesLabel → {Style["Area[mm2]", 30, FontFamily → "Times New Roman"],
    Style["Probability", 30, FontFamily → "Times New Roman"]}, TicksStyle →
    Directive[Bold, 25, FontFamily → "Times New Roman"], PlotStyle →
    ColorData[1, "ColorList"], Joined → True, PlotMarkers → {Automatic, 15}};
p = ListLogLogPlot[{data5, data55, data6, data65, data7, total}, option]

```